Giant aeolian dune size determined by the average depth of the atmospheric boundary layer

— Supplementary material —

B. Andreotti[1], A. Fourrière[1], F. Ould-Kaddour[2] A.B. Murray[3] and P. Claudin[1]

[1]Laboratoire de Physique et Mécanique des Milieux Hétérogènes, (PMMH UMR 7636 CNRS-ESPCI-P6-P7), 10 rue Vauquelin, 75231 Paris Cedex 05, France.

[2]Laboratoire de Physique Théorique, Université Abou Bekr Belkaid Tlemcen, Algeria.

[3]Nicholas School of the Environment and Earth Sciences, Center for Nonlinear and Complex Systems, Duke University, Box 90230, Durham, NC 27708-0230 USA.

———————

Table of contents:

1   Method: Measuring the average depth of the atmospheric boundary layer

In this supplementary method section, we show how the typical mixing height H can be determined from ground temperature measurements.

1.1   Aim of the approach

The main aim of the letter is to show the influence of the vertical structure of the atmospheric boundary layer (ABL) on the size of giant dunes. These dunes form over long periods of time (typically ten thousands years) and should thus be related to statistically averaged quantities. The detailed modelling of the atmospheric processes is very complex due to its intrinsic variability: e.g. nocturnal/diurnal cycles, daily variation of cloud cover and weather conditions, long term memory effects and seasonal evolution of the ABL, etc [5, 6]. Besides, the evolution of dunes is also an intermittent process determined by wind driven sand transport and thus sensitive to the wind regime (Fig. 5). To achieve a fully quantitative description of the problem, one would thus need to investigate the average effect of the ABL structure, adequately weighted by the wind strength and direction [7].

This is far beyond the current state of science for several reasons amongst which the lack of long time series of spatially resolved atmospheric data in desertic zones and the lack of ABL models valid on long time-scales. We show here that despite this complexity, a semi-quantitative description can be proposed (at least in the tropical desertic regions) from elementary scaling law arguments. For instance, figure 5 shows that the winds contributing most to sand transport have a velocity around 2 U_{th} and blow a significant fraction of time. This justifies to ignore the wind fluctuations and in particular the rare largest storms, in first approximation. In the same spirit, the description detailed below provides a way to average systematic daily variations as well as random weather fluctuations to get the typical ABL structure at the seasonal time-scale.
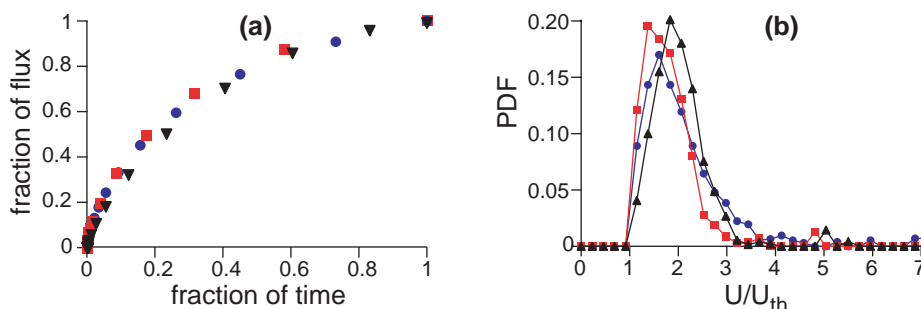

Figure 5: (a) Fraction of the overall aeolian sediment flux due to the largest winds, as a function of the fraction of time during which they blow. This parametric plot represents, on the vertical axis, the flux due wind speeds larger than U normalised by the total flux; The horizontal axis is the time during which the wind speed is larger than U normalised by the time during which the wind speed is larger than the transport threshold U_{th}. This cumulative distribution is almost the same for the three deserts shown here, Atlantic Sahara (Tan-Tan, ▲), Grand Erg Oriental (Ouargla, ●) and RubAlKhali (Sulayel, ■). However, the fraction of time during which there is transport ($U > U_{\text{th}}$ is respectively 45%, 32% and 25% on the ground and 65%, 69% and 44% on dune summits. Typically, half of the overall sediment flux is transported by the 25% more intense winds. The largest 1% storms, blowing one or two days per year, transport around 8% of the overall flux. (b) Probability distribution function (PDF) of the wind velocity U normalised by U_{th}. The PDF is weighted by the sediment flux the wind can transport: it measures the fraction of the overall flux transported by the winds of velocity U. The winds contributing most to the overall transport have a velocity between U_{th} and 3 U_{th}.
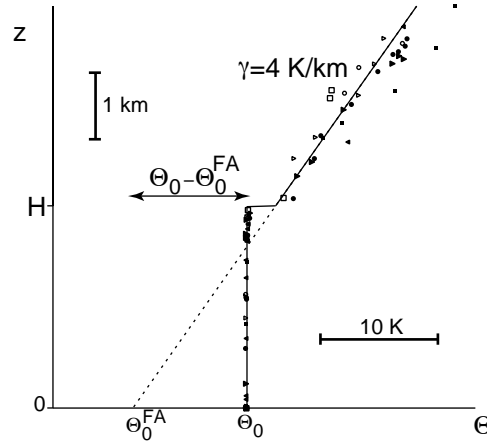
Figure 6: (a) Example of vertical profiles of the virtual potential temperature (IGRA data base [2], Ouargla, Algeria). The symbols correspond to different sounding dates: june 29th 1997 (○), july 7th 1997 (□), october 16th 1997 (△), october 25th 1997 (●), november 28th 1997 (■), february 1st 2000 (▲) and february 5th 2000 (▼). They have all been performed around 12 UTC/GMT. The profile below H is flat: $\Theta_v(z) \simeq \Theta_0$. Above the capping layer, the profile is fitted by a linear relation, giving the slope $\gamma \simeq 4\text{K/km}$ and the reference temperature Θ_0^{FA}.

We do not intend to provide a meteorological description which could account for local weather particularities and for the variability at the scale of days. Rather, we aim to understand and isolate the major physical mechanisms governing the ABL structure. More precisely, the depth of the ABL, averaged at the seasonal scale, turns out to be mostly determined by the ground temperature. Using available meteorological data, we show here that the identified scaling laws are robust and reliable for the giant dune formation problem.

1.2   Density profile

The typical vertical structure of the ABL in desert regions almost ideally fits the convectively driven situation described in text books [5, 6, 7]. As shown in figure 6, a well-mixed layer (ML) of thickness H lies below the stratified free atmosphere (FA). In between, the entrainment zone has a thickness negligible compared to H. The air density profile is roughly constant in the ML, and linearly stratified in the FA. We note by $\Delta\rho$ the density drop from the ML to the FA, which is much smaller than the reference density ρ_0. To the first order, the density profile can be approximated by:

$$\rho \;=\; \rho_0 \quad \text{for} \quad z < H, \tag{1}$$

$$\rho \;=\; \rho_0 - \Delta\rho + (z-H)\frac{d\rho}{dz} \quad \text{for} \quad z > H, \tag{2}$$

where the density gradient is a negative constant. The so-called Brunt-Väisälä frequency $N \equiv \sqrt{-g\frac{1}{\rho_0}\frac{d\rho}{dz}}$ is then also a constant and characterises the stability of the FA. The time-scale over which the depth H evolves is assumed to be large compared to the hydrodynamical and thermo-dynamical equilibration times.

1.3   Virtual potential temperature profile

It is usual in the atmospheric context to introduce the virtual potential temperature defined as

$$\Theta = T_v \left(\frac{P_0}{P}\right)^{R/C_p}, \tag{3}$$

where $P_0 = 10^5$ Pa is a reference pressure, $R = 8.31$ J/K the perfect gaz constant, C_p the air molar heat capacity and T_v is the virtual temperature defined with respect to the ordinary temperature as

$$\frac{T}{T_v} = 1 - \left(1 - \frac{M_w}{M_d}\right)\frac{e_{\text{sat}}(T_d)}{P}. \tag{4}$$

In this expression, e_{sat} is the saturated vapour pressure – e.g. given by Hylan and Wexler's fit [1] – and T_d is the dew point temperature; $M_w = 0.018$ kg/Mol and $M_d = 0.029$ kg/Mol are the molecular masses of water and dry air respectively. It is easy to sea that $d\Theta = 0$ for an air parcel experiencing an adiabatic transformation.

The equation of state of the air can be written as $\rho = \frac{P_0}{R_d\Theta}\left(\frac{P_0}{P}\right)^{R/C_p - 1}$, where $R_d \equiv R/M_d = 287$ m^{2}s^{-2}K^{-1}Mol^{-1}. In agreement with the classical Boussinesq approximation, we consider that the main variations of the density come from those of the temperature (and not the pressure) [8]. It follows that $\frac{d\rho}{\rho} \simeq -\frac{d\Theta}{\Theta}$. The Brunt-Väisälä frequency can therefore be expressed in terms of the potential temperature as

$$N^2 = g\gamma/\Theta, \tag{5}$$

where the temperature gradient $\gamma \equiv \frac{d\Theta}{dz}$ is a positive constant. Similarly to the density, the potential temprature vertical profile is then given by:

$$\Theta = \Theta_0 \quad \text{for} \quad z < H, \tag{6}$$
$$\Theta = \Theta_0 + \Delta\Theta + \gamma(z - H) \quad \text{for} \quad z > H. \tag{7}$$

The surface layer, dominated by the shear induced turbulent mixing, is not explicitly taken into account within these approximations. From the $z > H$ region, one can extrapolate the value Θ_0^{FA} of the virtual temperature on the ground:

$$\Theta_0^{\text{FA}} = \Theta_0 + \Delta\Theta - \gamma H. \tag{8}$$

Neglecting the temperature jump across the capping layer, this ideal picture leads to the following geometrical relation between ground temperature and mixing height:

$$H \simeq (\Theta_0 - \Theta_0^{\text{FA}})/\gamma. \tag{9}$$

The above vertical structure is used in section 7 for the aerodynamic calculation. We show below that this description, although not valid to describe the daily fluctuations of the ABL, provides the correct scaling laws for quantities averaged over few weeks.

1.4   Relation between mixing height and ground temperature

There is no available data base allowing a direct and systematic analysis of the potential temperature Θ, its vertical gradient γ, the corresponding Brunt-Väisälä frequency N, the capping height H and the temperature drop $\Delta\Theta$ at the crossing of the interface between the FA and the ML. The balloon soundings from the Integrated Global Radiosonde Archive (IGRA [2, 3]) provide some raw meteorological data. They are unfortunately rather sparse in time and with a poor vertical resolution in the mixing layer. We have focused on three places – Ouargla (31°55'N 5°24'E, Algeria), Sulayel (20°28'N 45°37'E, Saoudi Arabia) and São Luis (02°53'S 44°28'W, Brasil) – to process the IGRA data and extract the potential temperature measured on the ground Θ_0, the potential temperature gradient γ, the capping height H and the potential temperature extrapolated to the ground from a linear fit of the data in the FA region Θ_0^{FA}.

These quantities are plotted as a function of the day number in figure 7. Panels (a) and (b) show that although both Θ_0 and Θ_0^{FA} follow the seasonal changes, the variation amplitude of the latter is significantly smaller than that of the former. The most robust output is the temperature gradient (panel (d)): γ is almost constant ($\gamma \simeq 4$K/km) all year long and independent of the location, which means that the FA is only weakly affected by the heating of the ground, but rather is governed by atmospheric mechanisms on a large scale, in particular radiative transfers and
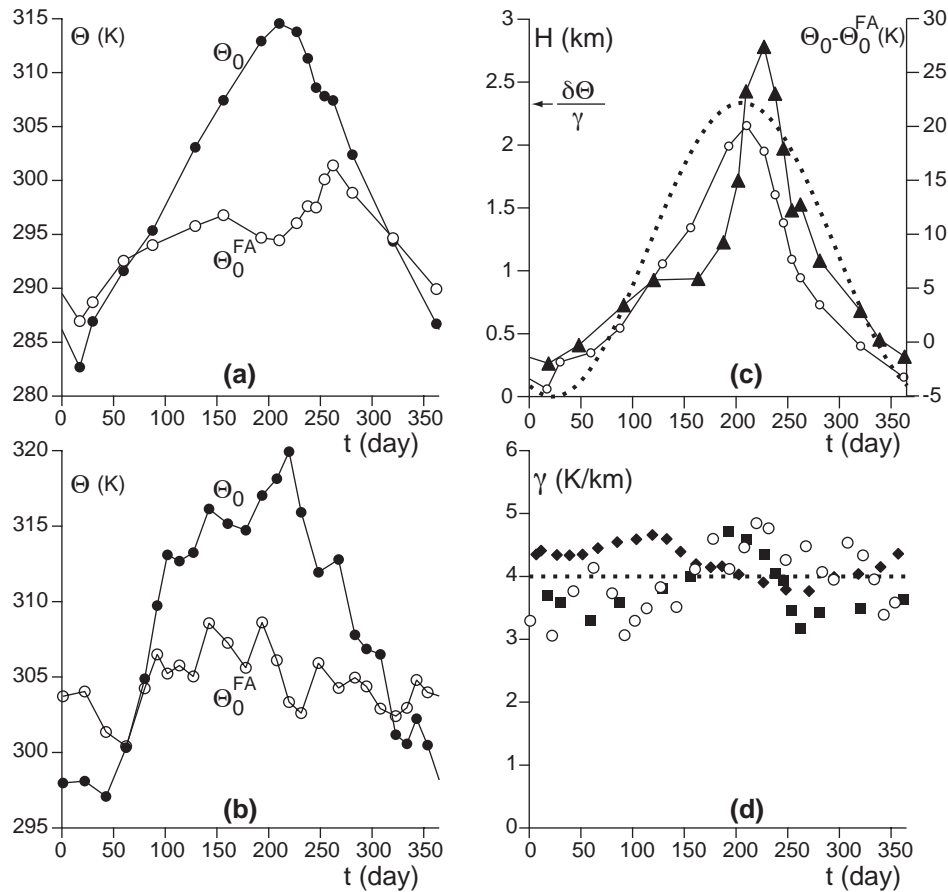
Figure 7: Meteorological data computed from balloon soundings [2] in three places: Ouargla (Algeria), Sulayel (Saoudi Arabia) and São Luis (Brasil). (a) Virtual potential temperature measured on the ground Θ_0 (•) and extrapolated to the ground from a linear fit of the data in the FA region Θ_0^{FA} (○), as a function of the day number, in Ouargla. Available data cover the time period june 1997 – may 2000 and have been averaged over a 10 day wide running window. (b) Same for Sulayel over the period october 1977 – december 1978. (c) Depth of the ML (▲) and ground temperature difference $\Theta_0 - \Theta_0^{\mathrm{FA}}$ (○), in Ouargla, as a function of the day number. The dashed line corresponds to the prediction of H by equation (12), whose parameters are determined by fitting the ground temperature time series (Fig. 8). The arrow shows the typical mixing height determined by $H = \delta\Theta/\gamma$. (d) Free atmosphere virtual potential temperature gradient γ in Ouargla (■), Sulayel (○) and São Luis (♦) as a function of the day number.

residual turbulent mixing. Other typical values determined from this analysis are: $N \simeq 0.01\mathrm{s}^{-1}$, $\Delta\Theta/\Theta_0 = \Delta\rho/\rho_0 \simeq 0.005$.

Finally, in panel (c), we display the mixing height H, averaged over 10 days, as a function of time. From the technical point of view, we average all the points obtained over several years whose acquisition dates coincide within 5 days. It is thus an ensemble average that mixes very different realisations, for instance sunny days where the convective layer reaches its maximum possible height (Eq. 9) but also cloudy days during which the convective layer does not develop. As expected, H is larger during summer time and almost vanishes in winter. Although not necessarily valid for individual profiles, we find that the average thickness of the ML follows very well the seasonal evolution of the temperature difference $\Theta_0 - \Theta_0^{\mathrm{FA}}$, averaged in the same way as H. These results thus support a simplified picture in which the FA is in a steady state, characterised
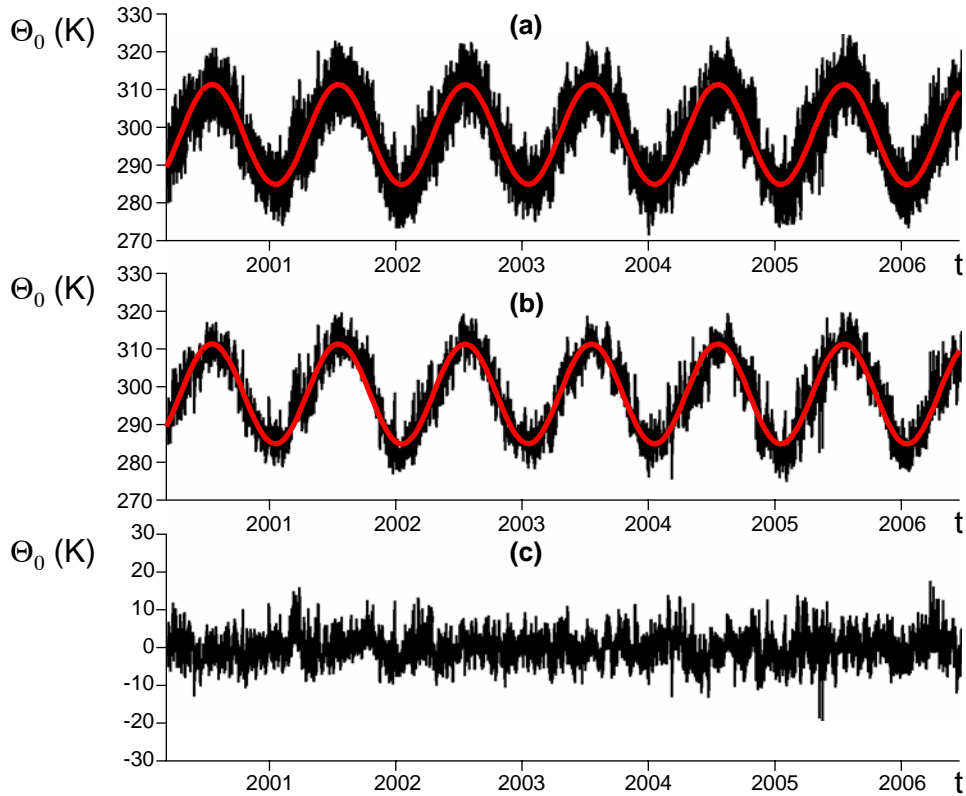
Figure 8: Ground virtual potential temperature versus time, in Ouargla, Algeria (airports weather data base [4]). The raw data are displayed in panel (a). In panel (b), the sinusoidal daily variations have been subtracted. The remainder has been fitted by equation (11) (red line). (c) Residual fluctuations, after substraction of both annual and daily sinusoidal variations.

by constant values of γ and Θ_0^{FA} (Fig. 6).

Because the meteorological database from sounding balloons such as those discussed above do not provide sufficiently frequent and precise data sets, we make use of ground temperature measurements to evaluate the seasonal variations of $\Theta_0 - \Theta_0^{\mathrm{FA}}$. These measurements are available from weather airport data bases in all relevant places in the world. This database provide daily measurements (temperature, pressure and humidity) performed with almost identical techniques in similar environments, see [4]. We have analysed more than a hundred such time-series in tropical deserts. They all show daily variations superimposed on quasi-sinusoidal annual variations (Figs. 8 & 9). Interestingly, the amplitude of daily variations does not depend much on the season. As a consequence, a good approximation of these data is given by:

$$\Theta_0 = \overline{\Theta} + \delta\Theta\sqrt{2}\sin(2\pi t + \varphi) + \mathcal{D}\sqrt{2}\sin(2\pi t/T_{\mathrm{day}} + \varphi_{\mathrm{day}}), \qquad (10)$$

where time t is expressed in years and T_{day} is 1 day. In this expression, $\overline{\Theta}$ is the average temperature and $\delta\Theta \equiv [\overline{(\Theta - \overline{\Theta})^2}]^{1/2}$ stands for the amplitude of variation of the ground temperature at the scale of the year (its rms value) and $\mathcal{D}$ at the scale of the day. In most places (but not e.g. in Brasil) the fitted phases φ and φ_{day} correspond to a maximum temperature in the mid-afternoon in the mid-summer. All the values corresponding to the different places investigated in this study are displayed in tables 1 and 2. The panels (a) of figures 8, 9 and 10 show raw data with the annual sinusoidal best fit

$$\Theta_0 = \overline{\Theta} + \delta\Theta\sqrt{2}\sin(2\pi t + \varphi), \qquad (11)$$

superimposed. Panels (b) show the same time series, once the sinusoidal fit of the daily variations
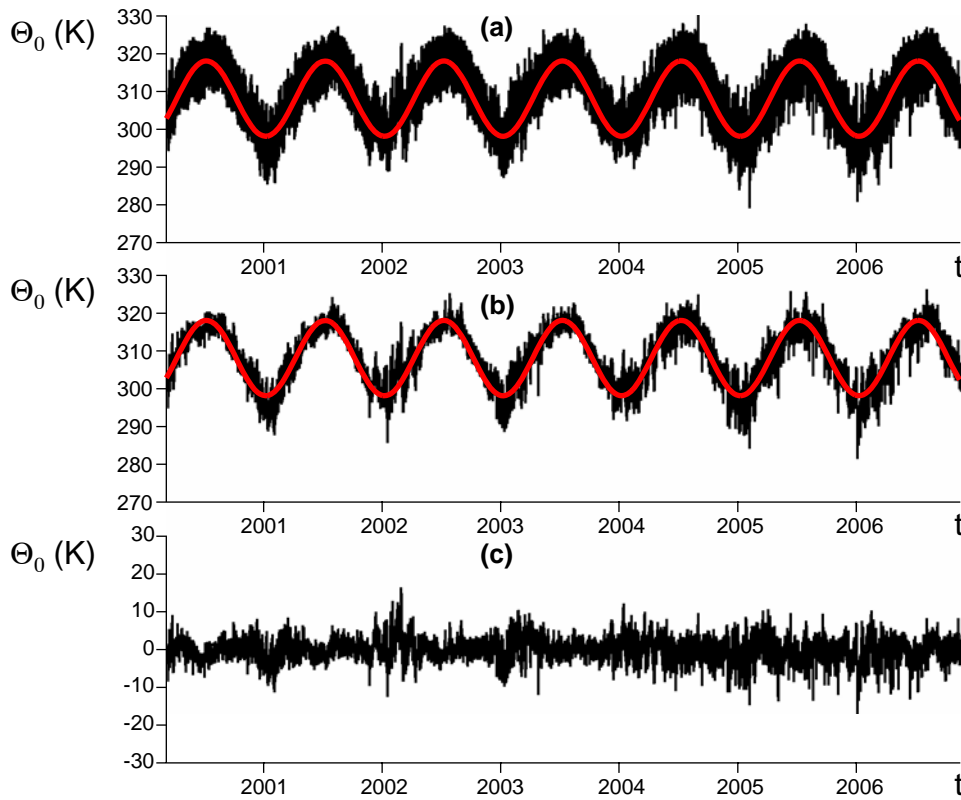
Figure 9: Ground virtual potential temperature versus time, in Sulayel, Saoudi Arabia. The raw data are displayed in panel (a). In panel (b), sinusoidal daily variations have been subtracted. The remainder has been fitted by equation (11) (red line). (c) Residual fluctuations, after substraction of both annual and daily sinusoidal variations.

is subtracted. Finally, panels (c) show the residual fluctuations i.e. the difference between the raw data and its fit by equation (10), which reflect the weather randomness. We hypothesise that giant dunes are insensitive to these stochastic variations, which can thus be ignored in the description of the problem.

Despite the extrapolated ground temperature Θ_0^{FA} is not perfectly constant in time, the panel (c) of figure 7 shows that the rms value of $\Theta_0 - \Theta_0^{\mathrm{FA}}$ is approximately equal to $\delta\Theta$. Since the convective ML is not necessarily present nor well developed (in particular at night), the average ML thickness H is weaker than expected if the ideal picture described in section 1.3 was true at each instant. Still, the fact that the mixing height can go higher for higher ground temperature is such a robust process that the geometrical law holds, within a prefactor:

$$H \sim \frac{\delta\Theta}{2\gamma}\left[1 + \sin(2\pi t + \varphi)\right]. \tag{12}$$

This estimate is in fair agreement with the meteorological data in Ouargla, see figure 7(c). The maximum of this curve, $\delta\Theta/\gamma$, gives a typical value of the thickness of the well-mixed layer, representative of the corresponding meteorological local conditions. This is the value that we use to investigate the scaling law of the giant dune size. Note that the annual average of the mixing height is in fact closer to $\frac{1}{2}\,\delta\Theta/\gamma$.
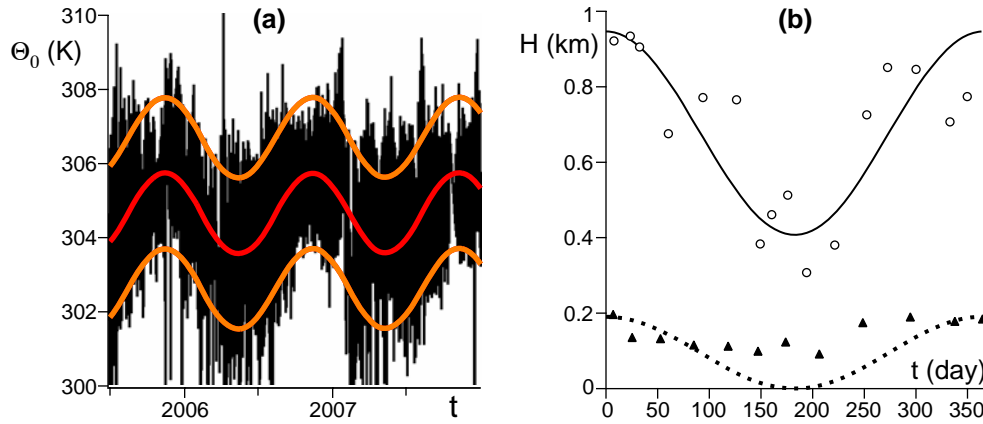
Figure 10: Ground virtual potential temperature versus time, in Parnaiba (02°55'S 41°36'W, same region as São Luis, Brasil). The raw data are displayed in panel (a). The red solid line is the best fit by a sinusoid (Eq. 11). The orange lines correspond to the maximum and minimum daily temperatures given by equation (13). (b) Average depth of the ML in Parnaiba as a function of the day number computed on the whole time series (▲) or conditioned by the existence of an inversion layer persistent after one night (○). The dashed line corresponds to the model equation (12), whose parameters are determined by fitting the ground temperature time series (a). Available data cover the time period january 1984 – july 1987. The solid line corresponds to the model equation (14), for the maximum mixing height.

1.5   Maximum vs average mixing height

To understand the robustness of the relation between mixing height and ground temperature, we summarise here the basic processes at work during annual and daily cycles. During the nocturnal cycle, the ground virtual potential temperature becomes smaller than that in the former ML – and that in the FA. As a consequence, the fluid gets stably stratified down to the ground: convection is blocked and the only remaining fluctuations come from mechanical turbulence i.e. inertial non-linear effects. While convection turbulence tends to homogeneise the virtual potential temperature Θ, mechanical turbulence tends to homogeneise the real temperature T and thus slowly restores stratification below the free atmosphere (Eq. 3). Still, the temperature profile in the morning most often keeps memory of previous days. During the next diurnal cycle, a turbulent heat flux from the surface into the atmosphere occurs whenever the ground temperature becomes larger than that of any layer above it. A new mixing layer develops whose maximum height is that for which the virtual potential temperature in the free atmosphere is equal to that of the ground, independently of the initial profile let after the night. Indeed, the turbulent heat flux would be suppressed if the ground was cooler than the FA. Equation (9) thus corresponds to this maximum height, reached after some transient. Under different weather conditions (e.g. clouds), the ground temperature can never sufficiently increase to induce strong convection and the mixing height remains very small.

Figure 10 illustrates this crude picture on an extreme example (coastal Brasil). Indeed, panel (a) shows there is almost no annual temperature variation ($\delta\Theta = 0.7$ K) due to the thermal regulation by the oceanic influence. Then, in comparison, the daily variations are rather important ($\mathcal{D} = 1.5$ K), the maximum and minimum temperature being well described by:

$$\Theta_{\pm} = \overline{\Theta} + \delta\Theta\sqrt{2}\sin(2\pi t + \varphi) \pm \mathcal{D}\sqrt{2}. \qquad (13)$$

Figure 10(b) shows the annual variations of the mixing height, computed from atmospheric soundings in two different ways. The bottom series of symbols (▲) corresponds to a value averaged over a 10 day wide running window, taking into account the whole available data (measured in the morning, at 12 UTC/GMT). This includes the frequent situation where the stratification extends

down to the ground: we have then set the mixing height to 0. The top series of symbols ($\circ$) is the same, but conditioned by the persistence of an inversion layer from the previous day i.e. when the profile is not stratified down to the ground. As for the Algerian case (Fig. 7 c), the average mixing height is in nice agreement with the prediction of equation (12). Still, the mixing height can grow to roughly 1 km, as shown by the conditional average. Following our analysis, H cannot be larger than the geometrical relation (9), evaluated for the ground maximum temperature Θ_+:

$$H_{\max} = \frac{\mathcal{D}\sqrt{2} + \delta\Theta\sqrt{2}\left[1 + \sin(2\pi t + \varphi)\right]}{\gamma} \, . \tag{14}$$

It can be observed that this relation fits quantitatively the data, which reinforces the strength of the theoretical argument for the maximum ABL depth (Eq. 9) is very strong. In other words, one can consider that the maximum is reached as soon as a mixed layer develops.

1.6 Dispersion relation of the waves propagating on the capping layer

We derive here the dispersion relation of the waves propagating on the capping layer (equation (1) of the letter). In the first approximation, the mixed layer and the free atmosphere are considered as two immiscible perfect fluids. Following the ABL structure previously described, the density of the ML is homogeneous and equal to ρ_0 and there is a density drop $\Delta\rho$ at the interface. The FA is stably stratified from the interface to infinity, with a constant Brunt-Väisälä frequency N defined by:

$$N^2 = -\frac{g}{\rho_0 - \Delta\rho}\frac{d\rho}{dz} \tag{15}$$

In the ML, the Euler equations read:

$$\partial_x u_x + \partial_z u_z = 0, \tag{16}$$
$$\rho_0\left(\partial_t u_x + u_x\partial_x u_x + u_z\partial_z u_x\right) = -\partial_x P, \tag{17}$$
$$\rho_0\left(\partial_t u_z + u_x\partial_x u_z + u_z\partial_z u_z\right) = -\partial_z P - \rho_0 g, \tag{18}$$

Linearising around the static reference situation, which is homogeneous in space and time, the general solution takes the form $e^{i\omega t + ikx + q_\downarrow z}$. The pressure disturbance $\tilde{P}$ is related to the vertical velocity by:

$$\rho_0\omega q_\downarrow u_z = ik^2\tilde{P}, \tag{19}$$
$$\rho_0 i\omega u_z = -q_\downarrow\tilde{P}, \tag{20}$$

In the limit of large kH, the vertical decay rate is related to the wavenumber by:

$$\frac{q_\downarrow}{k} = 1. \tag{21}$$

This means that the disturbances decay exponentially with the distance to the interface, with a rate equal to k. In the FA, we use the Boussinesq approximation [?]:

$$\partial_x u_x + \partial_z u_z = 0, \tag{22}$$
$$(\rho_0 - \Delta\rho)\left(\partial_t u_x + u_x\partial_x u_x + u_z\partial_z u_x\right) = -\partial_x P, \tag{23}$$
$$(\rho_0 - \Delta\rho)\left(\partial_t u_z + u_x\partial_x u_z + u_z\partial_z u_z\right) = -\partial_z P - \rho g, \tag{24}$$
$$\partial_t\rho + u_x\partial_x\rho + u_z\partial_z\rho = 0. \tag{25}$$

Linearising around the static reference situation, which is also homogeneous in space and time, the general solution again takes the form $e^{i\omega t + ikx + q_\uparrow z}$, now with:

$$(\rho_0 - \Delta\rho)\omega q_\uparrow u_z = ik^2\tilde{P}, \tag{26}$$
$$(\rho_0 - \Delta\rho)\left(N^2 - \omega^2\right)u_z = -iq_\uparrow\omega\tilde{P}, \tag{27}$$

which gives:

$$\frac{q_\uparrow}{k} = -\sqrt{1 - \left(\frac{N}{\omega}\right)^2}. \tag{28}$$

The interface position H follows the material velocity on both side of the interface:

$$\partial_t H = \lim_{z \to H^+} u_z = \lim_{z \to H^-} u_z \tag{29}$$

The last boundary condition is the continuity of pressure through the interface:

$$\lim_{z \to H^+} P = \lim_{z \to H^-} P \tag{30}$$

This leads to the following dispersion relation for the interfacial waves,

$$\omega^2 + \left(1 - \frac{\Delta\rho}{\rho_0}\right)\omega\sqrt{\omega^2 - N^2} = \frac{\Delta\rho}{\rho_0}gk, \tag{31}$$

valid for asymptotically large kH. Note that the generalisation for finite kH may be easily obtained. Introducing the phase velocity $c = \omega/k$, one recovers equation (1) of the letter. We can see that the waves can propagate, localised at the interface, when ω is larger than N. However, when $\omega < N$, an imaginary term appears, which means that the interfacial waves are damped. The waves are not localised anymore on the interface and internal waves are radiated.

In rivers, gravity waves can also propagate at the free surface. Their dispersion relation is the same, except that the upper region can be treated as vacuum ($\rho = 0$), i.e. $\Delta\rho = \rho_0$ and $N = 0$. As discussed above as well as in the letter, the density drop in the atmospheric case is much smaller ($\Delta\rho/\rho_0 \simeq 0.005$). In that case, it is also important to emphasise that, even if the waves are trapped on the capping layer, their propagation is influenced by the stratification of the whole FA: that is the reason for which the dispersion relation $\omega(k)$ depends on N.

In the section 7, we derive the disturbances induced by the presence of dunes on the atmospheric flow, including turbulence. The effect of the capping layer is interpreted in terms of standing interfacial waves.

Dune type and location	Coord.	λ (km)	Nearest weather station	Coord.	$\overline{T}$ $\overline{\Theta}$ (K)	δT $\delta\Theta$ (K)	$\delta\Theta/\gamma$ (km)
Star dunes (Rub' al Khali, Oman)	19°27' N 53°42' E	1.7	Sharurah (S. Arabia)	17°28' N 47°07' E	302 310	5.6 6.4	1.6
Star dunes (Erg Oriental, Algeria)	31°27' N 07°45' E	1.8	Hassi Messaoud (Algeria)	31°40' N 06°09' E	297 298	8.8 9.3	2.3
Star dunes (Erg Chebbi, Morocco)	31°09' N 03°59' W	2.0	Errachidia (Morocco)	31°56' N 04°24' W	293 304	8.2 8.7	2.2
Star dunes (Erg Oriental, Algeria)	31°27' N 07°45' E	2.2	Hassi Messaoud (Algeria)	31°40' N 06°09' E	297 298	8.8 9.3	2.3
Star dunes (Sonora, Mexico)	32°03' N 114°23' W	2.5	Altar (Mexico)	30°43' N 111°44' W	296 300	7.4 8.3	2.1
Longitudinal dunes (Shara, Mauritania)	21°07' N 09°41' W	1.1	Atar (Mauritania)	20°31' N 13°04' W	302 304	4.2 4.8	1.2
Longitudinal dunes, (Rub' al Khali, S. Arabia)	18°11' N 47°21' E	1.9	Sharurah (S. Arabia)	17°28' N 47°07' E	302 310	5.6 6.4	1.6
Longitudinal dunes (Namib, Namibia)	24°15' S 15°03' E	2.2	Hardap (Namibia)	24°32' S 17°56' E	294 308	5.6 5.9	1.5
Longitudinal dunes (Sahara, Mali)	24°09' N 04°45' W	2.3	Bordji B. Mokhtar (Algeria)	21°20' N 0°57' E	300 304	6.9 7.7	1.9
Longitudinal dunes (Erg Oriental, Libya)	27°54' N 11°45' E	2.8	In Amenas (Algeria)	28°03' N 09°38' E	296 302	8.0 8.6	2.1
Longitudinal dunes (Gobi, China)	39°58' N 92°34' E	2.8	Dunhuang (China)	40°09' N 94°41' E	284 295	11.7 13.1	3.3
Longitudinal dunes (Iran)	30°21' N 59°21' E	2.9	Nokkundi (Iran)	28°49' N 62°45' E	299 307	8.2 9.5	2.4
Transverse dunes (Coastal desert, Brasil)	02°37' N 42°57' W	0.2	Parnaiba (Brasil)	02°55' S 41°36' W	302 303	0.9 0.7	0.2
Transverse dunes (Coastal desert, Venezuela)	11°26' N 69°42' W	0.2	Coro (Venezuela)	11°25' N 69°41' W	302 303	0.4 0.4	0.1
Transverse dunes (Atlantic Sahara)	28°04' N 12°13' W	0.4	Las Palmas (Spain)	27°56' N 15°23' W	294 294	2.1 2.4	0.6
Transverse dunes (Coastal desert, Peru)	14°54' S 75°30' W	0.4	Pisco (Peru)	13°45' S 76°17' W	293 294	2.5 2.9	0.7
Transverse dunes (Coastal desert, Angola)	16°23' S 12°01' E	0.5	Mocamedes (Angola)	15°12' S 12°09' E	295 297	2.6 3.0	0.7
Transverse dunes (Coastal desert, Namibia)	25°45' S 14°55' E	0.7	Lüderitz (Namibia)	26°38' S 15°03' E	290 290	1.6 1.8	0.5
Transverse dunes (Algodones, USA)	32°49' N 114°59' W	0.9	San Diego (USA)	32°44' N 117°10' W	290 291	2.7 3.2	0.8
Transverse dunes (Sahara, Tunisia)	32°47' N 09°14' E	0.9	Remada (Tunisia)	32°19' N 10°24' E	294 297	6.9 7.4	1.9

Table 1: Mean dune wavelength λ measured in different locations. From the airport weather station the closest to each site, we get the average ground (resp. ordinary and virtual potential) temperatures $\overline{T}$ and $\overline{\Theta}$ as well as the rms amplitude δT and $\delta\Theta$ of their annual variations. The last column gives an estimation of the typical mixing depth computed as $H \simeq \delta\Theta/\gamma$ with $\gamma = 4$K/km. These data are displayed in figure 2(a) of the letter.

Transverse dunes (Sonora, Mexico)	31°48' N 113°51' W	1.4	Puerto Penasco (Mexico)	31°18' N 113°33' W	296 297	6.6 7.6	1.9
Transverse dunes (Iran)	30°47' N 59°37' E	1.7	Nokkundi (Iran)	28°49' N 62°45' E	299 307	8.2 9.5	2.4
Transverse dunes (East Pakistan)	28°04' N 65°10' E	1.7	Khuzdar (Pakistan)	27°50' N 66°38' E	296 310	7.1 8.3	2.1
Transverse dunes (Erg Occidental, Algeria)	30°07' N 0°43' E	1.8	Timimoun (Algeria)	29°15' N 0°17' E	298 301	8.9 9.6	2.4
Transverse dunes (Ming Shashan, China)	40°02' N 94°42' E	1.9	Dunhuang (China)	40°09' N 94°41' E	284 295	11.7 13.1	3.3
Transverse dunes (Algeria)	29°12' N 02°35' E	1.9	Tindouf (Algeria)	27°40' N 08°08' W	297 301	7.3 8.0	2.0
Transverse dunes (Great sand sea, Libya)	28°32' N 23°10' E	2.1	Siwa (Egypt)	29°12' N 25°29' E	296 296	6.6 7.3	1.8
Transverse dunes (Afghanistan)	30°35' N 65°40' E	2.2	Kandahar (Afghanistan)	31°30' N 65°51' E	295 306	8.0 9.1	2.3
Transverse dunes (North Taklamakan, China)	40°11' N 84°56' E	2.7	Kuqa (China)	41°43' N 82°57' E	284 294	11.5 12.9	3.2
Transverse dunes (South Taklamakan, China)	37°56' N 82°28' E	3.0	Andir (China)	37°56' N 83°39' E	285 297	11.2 12.9	3.2
Transverse dunes (East Taklamakan, China)	40°18' N 87°05' E	3.0	Ruoqiang (China)	39°02' N 88°10' E	286 294	12.3 13.6	3.4
Transverse dunes (East Badain Jaran, China)	38°38' N 104°59' E	3.2	Yunchuan (China)	38°29' N 106°13' E	283 294	10.9 12.4	3.1
Transverse dunes (West Badain Jaran, China)	40°04' N 102°13' E	3.4	Ejin Qi (China)	41°57' N 101°04' E	283 292	13.6 14.8	3.7
Snow giant dunes (Antarctica)	80°47' S 124°30' E	2.7	Vostok (Antarctica)	78°27' S 106°52' E	219 252	11.8 15.4	3.5

Table 2: Database continued.

2 Method: Measuring giant dune wavelength

In this section, we show the equivalence between four techniques that allow to measure the wavelength λ_g of giant dune patterns.

2.1 Fourier transform

The theory proposed for the scale of giant dunes is based on the aerodynamical calculation of the flow around dunes, which is local in the Fourier space and thus non-local in the physical space. It means that the giant dunes are under the influence of their neighbours even several ranks of dunes away. Thus, giant dunes should not be thought of as independent objects and the relevant quantity is a wavelength in the Fourier sense i.e. an average over a large spatial extent.

   We have performed Fourier analysis of the digital elevation model (DEM) of a star dune field in the Grand Erg Oriental (Algeria), which is one of the most subtle to analyse. It reflects the relative amplitude of the sinusoidal modes composing the pattern. This spectrum, displayed in figure 11 presents a central peak, which corresponds to the average altitude, surrounded by two peaks of very high amplitude (violet contours), four positive peaks (blue contours) and two negative peaks of lower amplitude (green contours). This corresponds to a complex pattern, hybrid between a hexagonal lattice (six positive peaks on a circle) and a parallelogram lattice (two positive and two negative peaks). These peaks correspond to the wavelengths of well-defined superposed modes. This organisation suggests a formation of these star dunes by secondary destabilisation
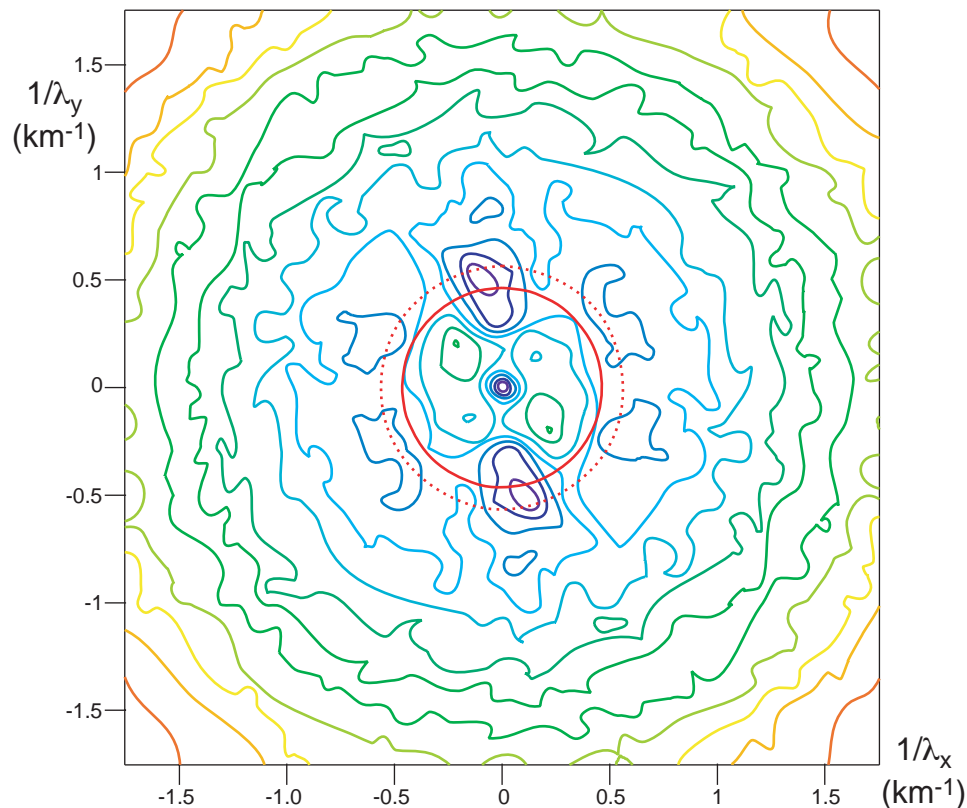

Figure 11: Fourier transform of star dune profiles of the Grand Erg Oriental obtained by a digital elevation model. For comparison, the wavelengths determined from the histograms of dune spacing along the principal directions of the pattern is shown by the red circles ($\lambda = 2.16$ km and $\lambda = 1.77$ km).

of longitudinal dunes, in which there are two dominant wavelengths, one along the longitudinal crests and the other crosswise. It is consistent with the the values of λ (red circles in figure 11) found using the mean dune spacing in these directions (solid line, $\lambda = 2.16$ km and dotted line, $\lambda = 1.77$ km, see table) or the structure function (see below).

2.2   Image auto-correlation

In practice, the Fourier transform directly applied on aerial pictures gives a spectrum that is too noisy to safely extract wavelengths. One can alternatively compute the correlation function of such an image. We recall that the correlation function is nothing but the Fourier transform of the Fourier spectrum. Still, as it averages over space, it is a smooth function that presents a well-identified peak at λ. An example of such an analysis, performed on longitudinal dunes, is displayed in figure 12. It presents a clear anti-correlation at 850 m which comes, on the image, from the succession of shadow and sunny zones as well as a positive correlation peak at $\lambda = 1700$ m. Although in principle, the maximum of correlation only coincides to a Fourier peak for a purely sinusoidal pattern, they give in practice similar values for the wavelength of the dominant mode.

2.3   Dune spacing

The maximum of image correlation corresponds to the situation for which, on the average, the displaced image of a rank of dunes best fits that of the next rank. So, it is similar in principle to the average spacing between neighbouring dunes. In the case of transverse and longitudinal dunes, this distance is measured between consecutive crests. For star dunes, one measures the distance between neighbouring dunes as shown in figure 13(b). One can then compute the histogram of these distances (see figure 13(a)), and define λ as the averaged value. As in most self-organised patterns presenting a well-defined wavelength, the width of the dune spacing distribution is of the order of its average λ, due to presence of dislocation-like defects. Comparing the average spacing with the wavelength computed by Fourier or correlation techniques, it turns out that these methods are equivalent in practice. The spacing analysis has the advantage of being insensitive to the lighting-induced heterogeneities of aerial photographs.

2.4   Structure function

The computation of the dune spacing histogram in the case of star-dunes hides a slight ambiguity: the results depend on the definition of neighbours. One can for instance use Voronoi tessellation or fix the number of neighbours. A more objective analysis is based on the so-called two-point structure function $g(r)$. Using the data set of individual dune spacings, one determines the probability to find a dune at a distance r from another dune, whatever the direction. As shown in figure 14, this function vanishes as $r \rightarrow 0$, rises to a maximum at some distance, and eventually reaches a plateau at large r. The maximum of probability coincides with the previous determinations of λ (vertical lines in figure 14).
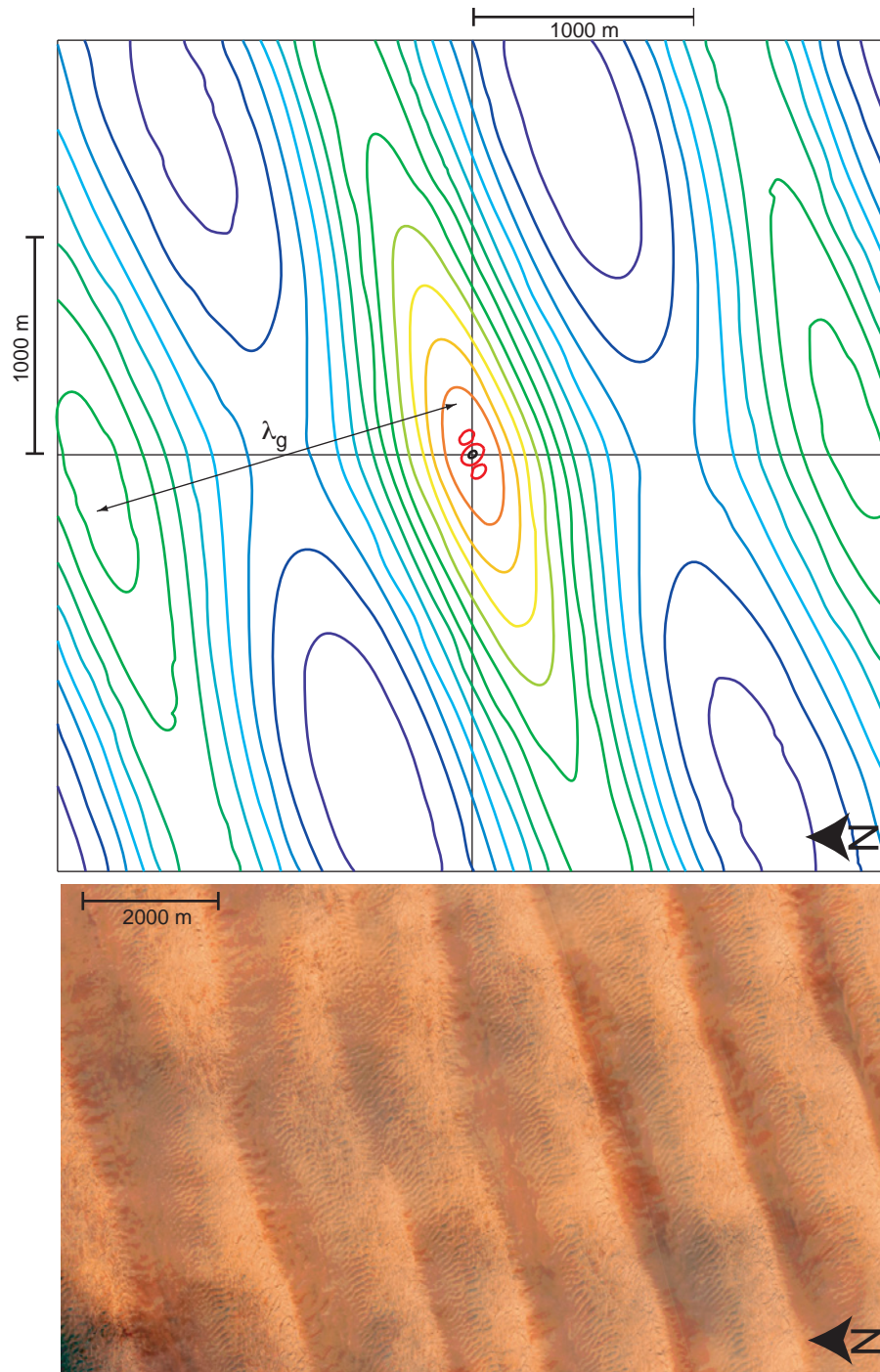
Figure 12: Correlation function of a color aerial image of longitudinal giant dunes in Rub al Khali. The axis are in meters. The levels of the iso-contours have been chosen to show the local maxima. Black and red correspond to a high positive correlation and blue to negative correlation. Two well-separated length-scales appear at 1700 m and 85 m, with no local maximum of correlation in between. The small wavelength corresponds to the linear destabilisation in between the ranks of dunes, due to the slow secondary winds.
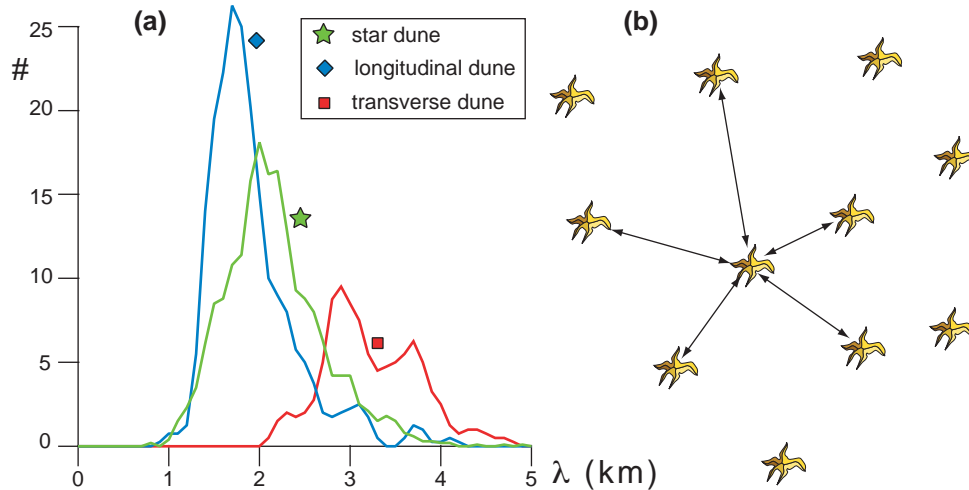
Figure 13: (a) Histograms of giant dunes spacing in some of the regions shown in figure 1: The star dunes (green symbols) are in Grand Erg Oriental (Algeria); the longitudinal dunes (blue symbols) are in Rub al Khali (Saoudi Arabia); the transverse dunes (red symbols) are in Badain Jaran (China). (b) Definition of the distance between neighbouring dunes (in the Voronoi sense) for the case of star dunes.
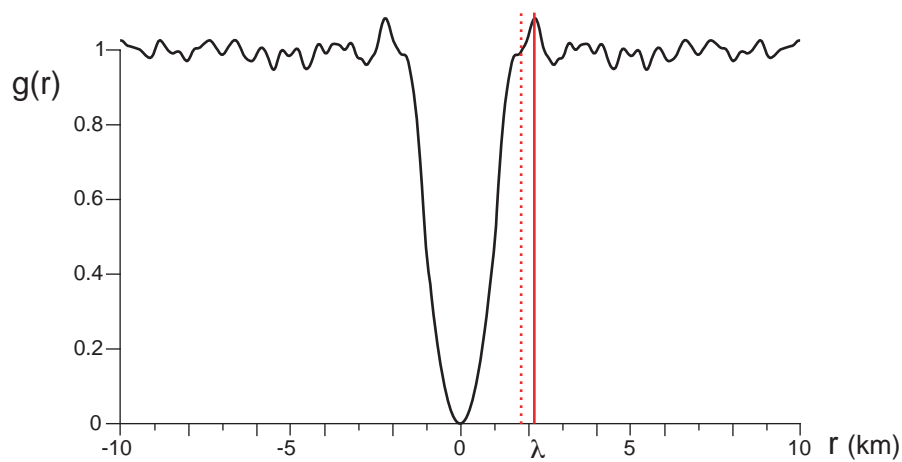

Figure 14: Two point structure function of the Grand Erg Oriental (star dunes). The wavelengths determined from the histogram of the dune spacing along the principal directions of the pattern is shown by the red lines ($\lambda = 2.16$ km and $\lambda = 1.77$ km, see also the corresponding circles in figure 11).

3   Capping layer waves

3.1   Visualisation of the waves in the field

Figure 15 presents direct evidence of the existence of rather low inversion layers (at the beginning of spring) and of the propagation of surface waves, similar to that on the free surface of a river. The star dune visible in the picture is located in the Grand Erg Oriental (Algeria) in the middle of an oil field zone. One can visualise the propagative waves above the dunes with the smoke coming from a close gas flare and stored below the capping layer as there is no mixing in the free atmosphere. Thus, the smoke directly shows this interface. It should be emphasised that the waves visible in this picture are not standing waves excited by the dune: they are propagative waves excited upwind of the dune by the flare.

3.2   Coastal dunes

Figure 16 is an aerial picture of the transverse dunes of Atlantic Sahara where we have studied in the field the interaction between superimposed dunes and the subsequent pattern coarsening (see fig. 4). It is also the place where the mega-barchans of figure 1(b) and 23 form. It provides evidence of the relation between the giant dunes and the atmospheric boundary layer. It can be observed that the giant dune scale is barely emerging in the first few ranks downwind of the sandy beach, develops further inland and eventually generates mega-barchans. The wavelength (~ 400m) nicely corresponds to the capping layer height (figure 2).

The orientation of the these giant dunes provides direct evidence that they are associated with the capping layer waves. Indeed, the crests of the superimposed dunes are perpendicular to to the very stable trade wind direction but the giant dune crests (red lines) deviates by $35°$ from this expectation. They are in fact parallel to the shoreline. The transition between the ocean and the land is a strong thermic perturbation that induces standing waves on the capping layer whose phase is related to the distance to the shoreline along the wind direction. What we see is the signature of these waves imprinted into the dune relief.
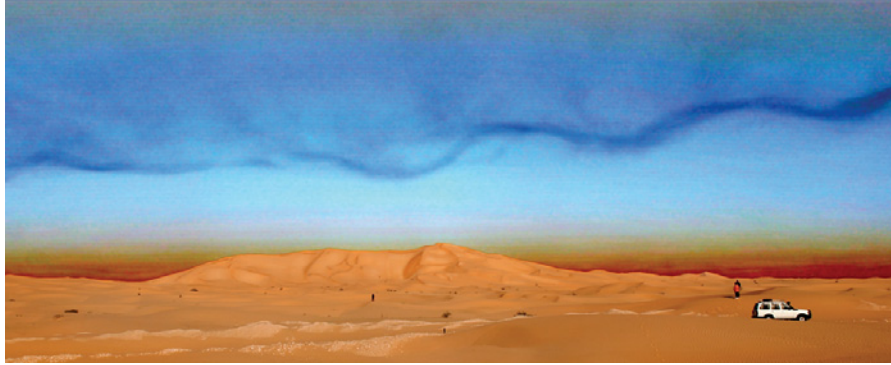
Figure 15: Visualisation by smoke of the waves propagating on the capping inversion layer above star dunes. The sky has been selectively contrasted by subtraction of the mean luminosity gradient.
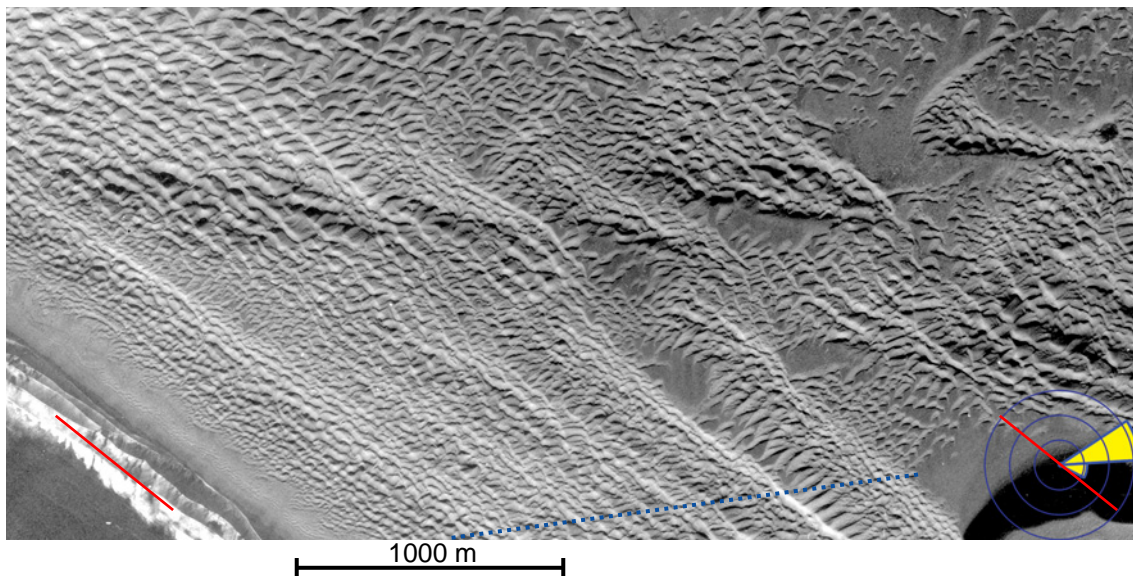

Figure 16: Transverse giant dunes in the same zone as in figure 23 (Atlantic Sahara). The ranks of dunes are parallel to the shore-line (red line), visible in the bottom left corner, and not perpendicular to the dominant trade winds (yellow sand rose). The dotted line in blue shows the section studied in fig. 4 of the letter.

4   Dune length-scale separation and pattern coarsening

In this section, we demonstrate that dune fields robustly exhibit the presence of an inner length-scale λ_s corresponding to elementary dunes and an outer length-scale λ_g corresponding to giant dunes. The key result of the letter is that the scaling-laws followed by these two length-scales are different because they are not selected by the same physical processes: one is related to sediment transport and the other to the atmospheric mixing height. We show that the presence or absence of structures at a scale between λ_s and λ_g depends on the type of analysis performed.

4.1   Aerial pictures

Looking at an aerial picture such as those of figures 17, 18, 19 and 23, one notices mostly the alternation of stoss slopes and avalanche slip faces at small wavelength, and the large scale relief on which they are superimposed. The inner elementary length-scale of the problem, governed by sand flux saturation length [9, 10, 11], is the length at which a flat bed destabilises. The outer length-scale is the kilometre scale wavelength discussed in this letter. The only places where the formation of elementary dunes is inhibited are just downwind of large slip-faces, due to screening.

In figures 17 and 23, which correspond to unimodal wind regimes, one can clearly see the superimposed small structures on the stoss side and the flanks of the mega-barchan and barchanoid giant dunes. Along the giant dune stoss slope, some coarsening (an increase of the wavelength) of the superimposed pattern is noticeable. A similar observation can be made in the case of star dunes formed by multi-directional winds (figure 18): the average distance between the dune summits, even considering the case of emerging star dunes, is much larger than the typical size of the superimposed structures. A progressive coarsening of the superimposed dunes is also visible in this photograph, with slip-faces getting larger closer to the star dune summits. Finally, figure 19 is interesting because we clearly see that the giant dune crest is in fact composed of numerous small scale slip-faces. In addition, small scale dunes also develop in the inter-crest region. In contrast to the case of transverse dunes, they are transverse to giant dunes, showing the existence of these longitudinal channelised secondary flows sufficiently strong to transport sand.

4.2   Correlation

In order to quantify the visual impression of scale separation between small superimposed and large structures, one can perform an auto-correlation of an aerial photo. One computes the correlation between the image and a copy of it, shifted by some distance, as a function of the displacement vector between the two. Positive and negative peaks of this function reveal the presence or the absence of a structure at the corresponding scale. A few examples are displayed here. In figure 20, we show a test case of this correlation analysis run on a photo of transverse dunes in coastal Angola. Two correlation peaks appear at 15 m and 530 m with no peak in between. This means that these two length-scales, which correspond to λ_s and λ_g objectively exist but also that the coherence length of the small scale pattern is very small. A similar analysis has been performed on photos of longitudinal dunes in Rub al Khali (figure 12), transverse dunes in the Taklamakan desert (figure 21) and giant dunes in Tunisia (figure 22). In the latter case, the analysis reveals a transverse pattern, resulting mostly from the orientation of the sun. The pattern symmetry, visible at the small scale (a square lattice pattern), is much more explicit in the picture (see also section 5).

4.3   Heights of secondary slip faces

The correlation technique quantifies what can be seen by eye. It is sensitive to the rhythmic succession of shadow zones behind slip-faces and not to slip-face relief. Figure 23 compares the picture of a mega-barchan to a longitudinal profile $z(x)$ measured in the field using combined GPS and geometrical data. In particular, the height δz of superimposed structures (with (brown) or without (orange) slip-faces) has been directly measured (see panel c). The horizontal and

vertical axes show considerably different pictures. On the one hand, the horizontal spacing between superimposed structures is never much larger than $\lambda_s \sim 25$ m. We have directly observed the formation of nascent structures in flat zones, as well as their propagation, the growth of their amplitude, and the nucleation of slip-faces as their amplitude becomes sufficient. In figure 23(c), these nascent structures correspond to the series of data points at meter scale amplitude (i.e. close to the axis $\delta z = 0$), visible all along the giant dune. On the other hand, the height of slip-faces are continuously distributed: there is no gap between the elementary dunes and the larger slip-faces. Moreover, the size of major slip-faces increases all along the mega-barchan. Taken together, the vertical and horizontal pictures show that pattern coarsening takes place in the course of propagation of secondary structures, but also that the elementary scale is regenerated. Having followed for five years the evolution of barchans in the Atlantic Sahara, we have directly observed many occurrences of these mechanisms, depicted in figure 24. We expect them to be also responsible for the formation of other types of giant dunes (e.g. figure 25).

4.4   Wavelet transform

We use a wavelet analysis to decompose giant dune relief into sub-structures at different scales. The principle of this method is explained in figure 26 for a particular scale. The full result of this decomposition is presented in figure 4 of the letter. It reveals that the giant dune is composed of a continuum of length-scales between the two extremes, λ_s and λ_g.

4.5   Pattern coarsening in the case of objects interacting with their first neighbours

We reproduce here the argument proposed by Anderson et al. [15] for a series of objects (here these objects would be dunes) exchanging mass with their first neighbours. These objects, labelled by i, can be parametrised by their size λ_i. Then, their height $a(\lambda_i)$ and their mass $m(\lambda_i)$ as functions of this size. It is assumed that the mass transfer between neighbours always goes from the highest one to lowest one. The equation of evolution of the mass can be written under the form:

$$\frac{dm(\lambda_i)}{dt} = 2\mathcal{F}(a(\lambda_i)) - \mathcal{F}(a(\lambda_{i+1})) - \mathcal{F}(a(\lambda_{i-1})) \tag{32}$$

where $\mathcal{F}$ is an increasing function of height which describes the rate at which mass is transferred from the lowest to the highest dune. Assume that there is a homogeneous field of objects having all the same size λ_{eq}. Expanding the equation of evolution at the first order in $\tilde{\lambda}_i = \lambda_i - \lambda_{\text{eq}}$, we get:

$$m'(\lambda_{\text{eq}}) \frac{d\tilde{\lambda}_i}{dt} = -a'(\lambda_{\text{eq}})) \mathcal{F}'(a(\lambda_{\text{eq}})) \left[\tilde{\lambda}_{i+1} + \tilde{\lambda}_{i-1} - 2\tilde{\lambda}_i \right] \tag{33}$$

This is the linear stability equation for the space discretised diffusion equation. The pattern is thus stable if $a'(\lambda_{\text{eq}})) \mathcal{F}'(a(\lambda_{\text{eq}}))/m'(\lambda_{\text{eq}})$ is negative and exhibits coarsening otherwise. The first time this occurs is right at the maximum of the curve $a(\lambda)$.
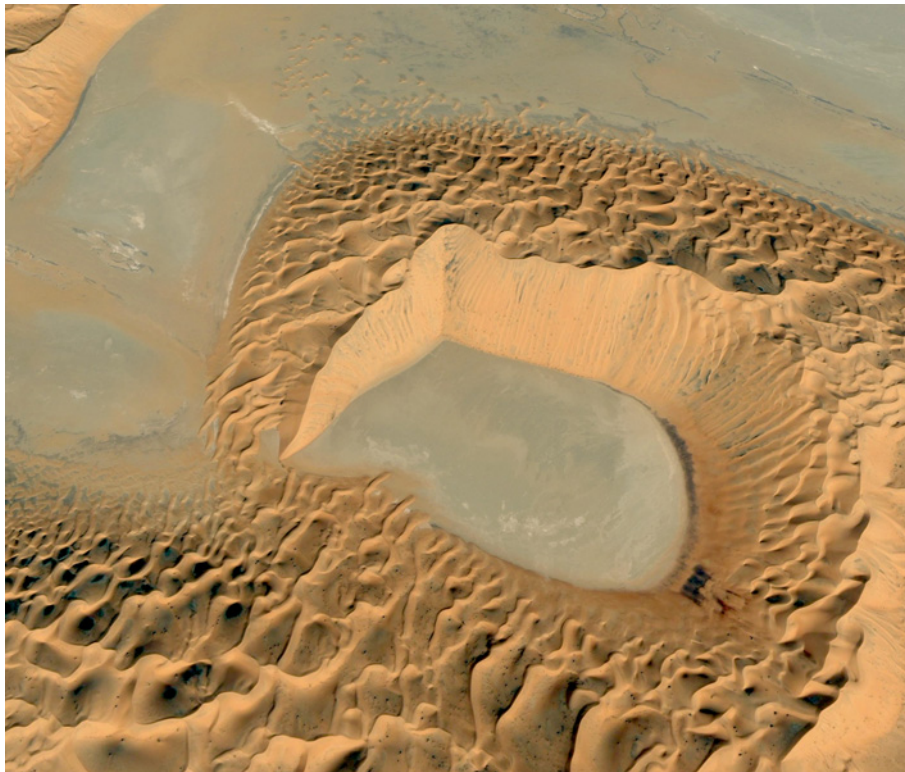
Figure 17: Barchanoid giant dunes of Rub' al Khali. The size of the photo is around 2km.
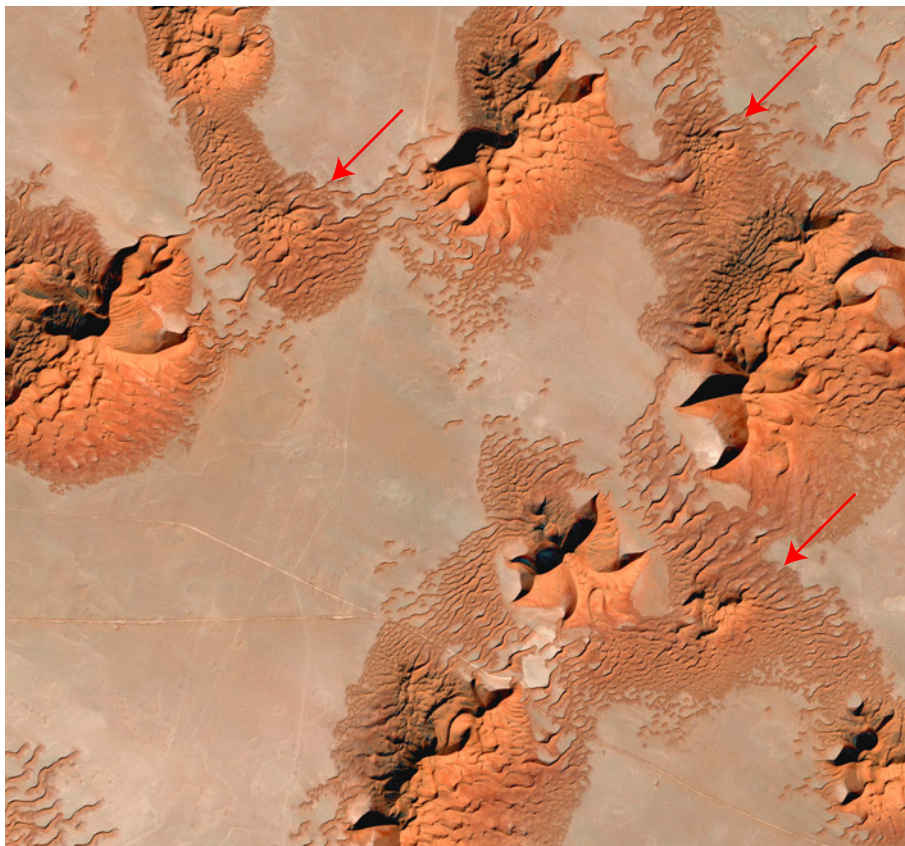
Figure 18: Star dunes in Rub' al Khali desert. The size of the photo is around 3km. Note few emerging star dunes in the middle of the small scale dune field (red arrows).
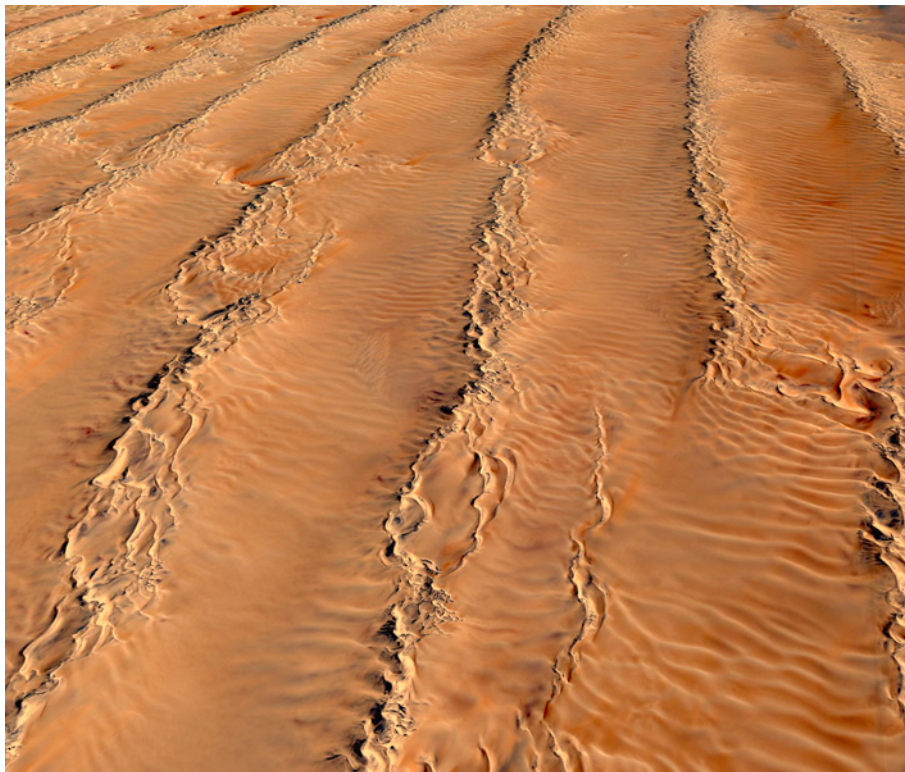
Figure 19: Longitudinal dunes in Namibia. The typical distance between two neigbouring dunes is 2km.
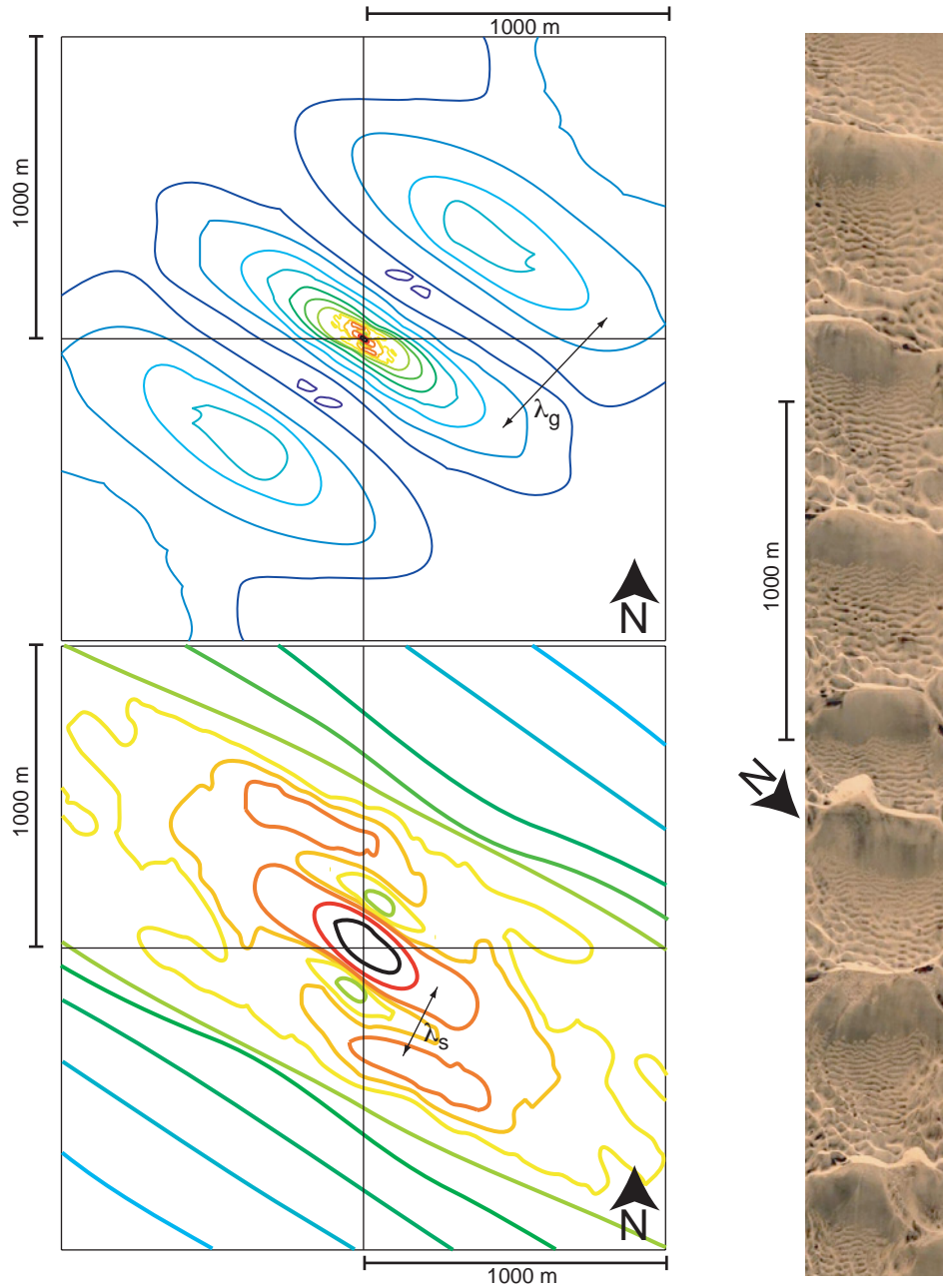
Figure 20: Correlation function of a color aerial image of coastal transverse giant dunes in Angola. The levels of the correlation iso-contours have been selected to show the local maxima. Black and red correspond to high correlation and dark blue to low correlation. The elongated iso-contours indicate a quasi-2D structure. The local maximum (light blue coutour) indicate a quasi-periodicity of wavelength λ_g around 530 m. The bottom panel is an enlargement of the top one by a factor of 10 and reveals the secondary maximum associated to the superimposed dunes (orange elongated contour), at $\lambda_s = 15$ m. The best correlation is actually obtained along a diagonal direction. This indicates a transverse modulation of secondary slip-faces due to a secondary wind direction. Note also the minimum of correlation (green contour) that comes from the good contrast of the image between stoss-slopes and slip faces. There no local maximum of correlation in between λ_s and λ_g.
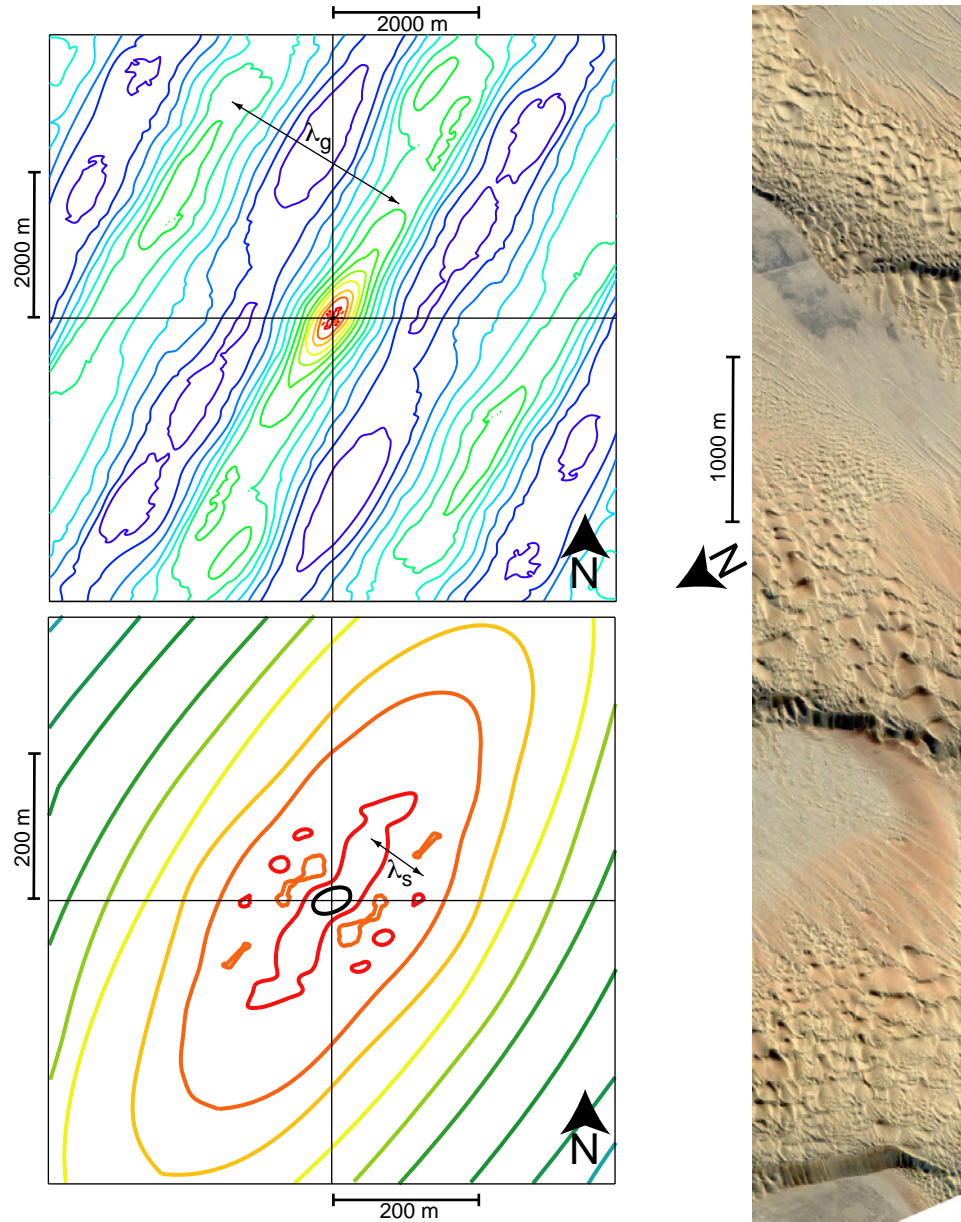
Figure 21: Correlation function of a color aerial image of transverse giant dunes in the Taklamakan desert (China). The levels of the correlation iso-contours have been chosen to show the local maxima. Black and red correspond to high correlation and dark blue to low correlation. The very-elongated contours indicate a nearly pure 2D transverse structure. Two local minima (blue contour) and one local maximum (green contour) are visible, revealing a periodicity of wavelength λ_g. The bottom panel is an enlargement of the top one by a factor of 10 and reveals the secondary maximum (red contours) associated with the superimposed dunes. Note that the orange contours correspond to local minima.
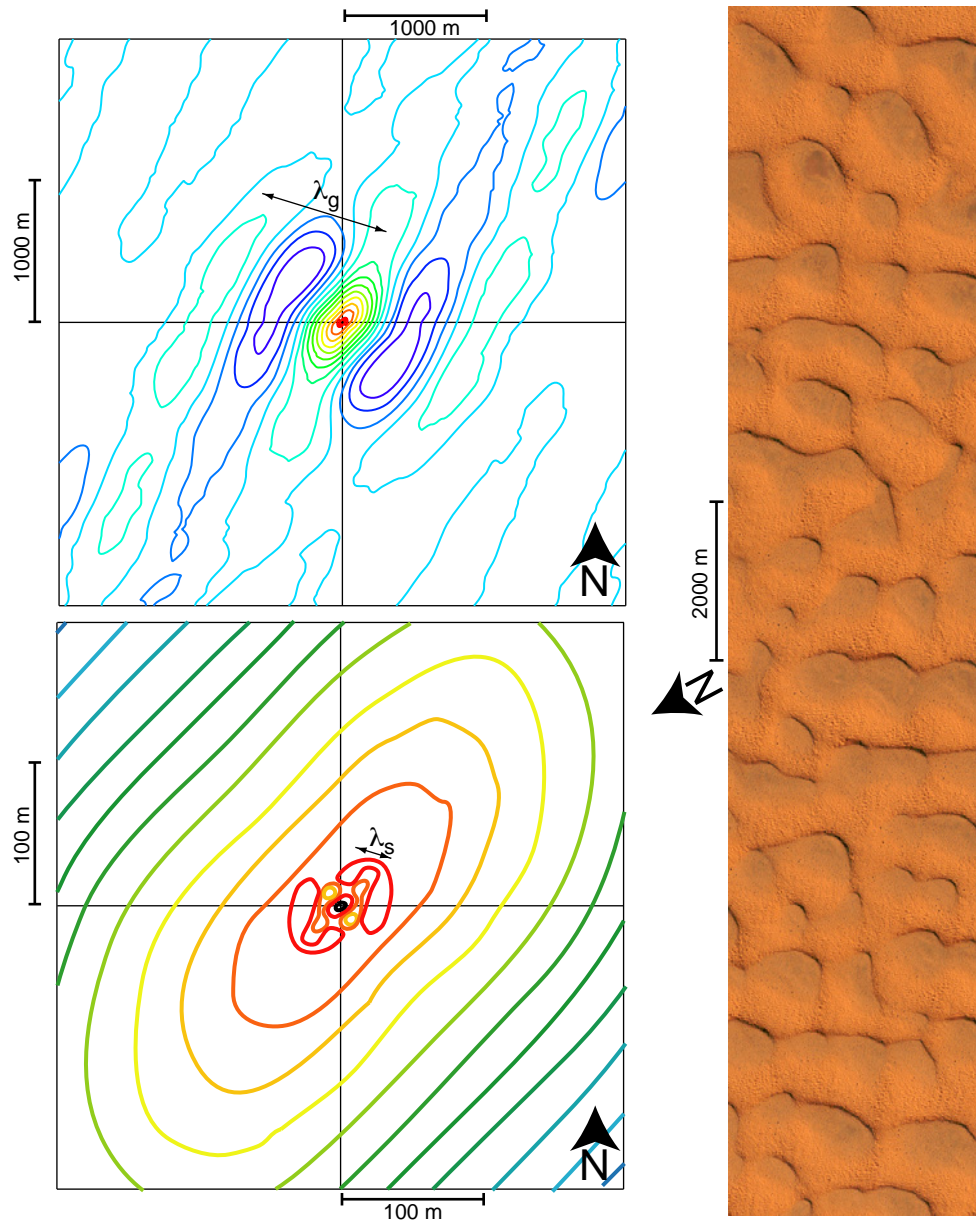
Figure 22: Correlation function of a color aerial image of giant dunes in Tunisia. The levels of the correlation iso-contours have been chosen to show the local maxima. Black and red correspond to high correlation and dark blue to low correlation. The elliptic contours correspond to a quasi-2D pattern. There are well defined secondary peaks that correspond to a minimum (dark blue) and to a maximum (light blue) of correlation. An asymmetry is visible that corresponds to the secondary modulation of the giant dunes. However, the sun angle creates darken shadows in one direction, contributing to this asymmetry. The bottom panel is an enlargement of the top one by a factor of 10 and reveals the secondary maxima (red contours) associated with the superimposed dunes. Four local maxima of correlation are visible, which reflect a square lattice structure at the scale λ_s.
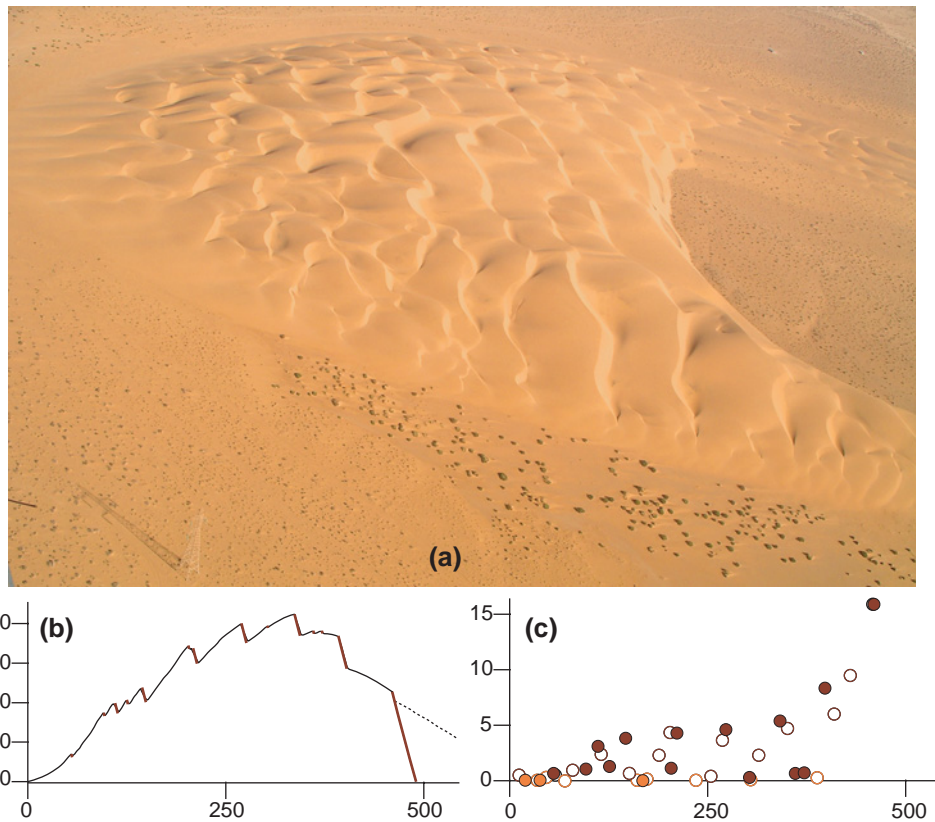
Figure 23: (a) Mega-barchan in the Atlantic Sahara. Its width is around 600m. (b) and (c) Amplitude of the superimposed structures modulating the surface of the mega-barchan shown in figure 1; brown symbols represent slip faces, while orange ones represent low waves without slip faces. Open circles are data collected in September 2004, and filled circles are from April 2007. Panel (b) shows the profile measured in 2007 (all distances in meters). The dotted line represents the approximate profile of the horns.
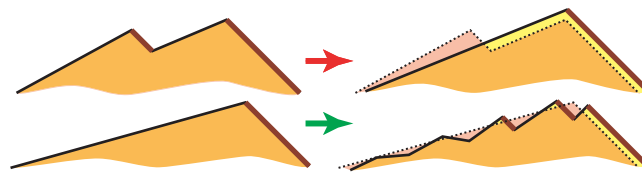

Figure 24: Schematic depiction of the different dynamical mechanisms governing the evolution of the superimposed dunes, as observed in the field. A sufficiently long flat surface destabilises to form dunes at the elementary wavelength (Green arrow). As small dunes propagate faster than large ones, they catch up with them and, when their slip faces coincide, amalgamate into a larger structure (Red arrow). When the wind makes an angle with the slip faces, the secondary flow inside the recirculation bubble is often sufficient to induce erosion at the foot of the slip face and deposition at the following crest. These three dynamical mechanisms result in the coarsening of the superimposed pattern along the slope of giant dunes.

Figure 25: Aerial photograph of a small star dune near Hassi-Messaoud (Algeria) apparently growing in an area covered by small dunes.
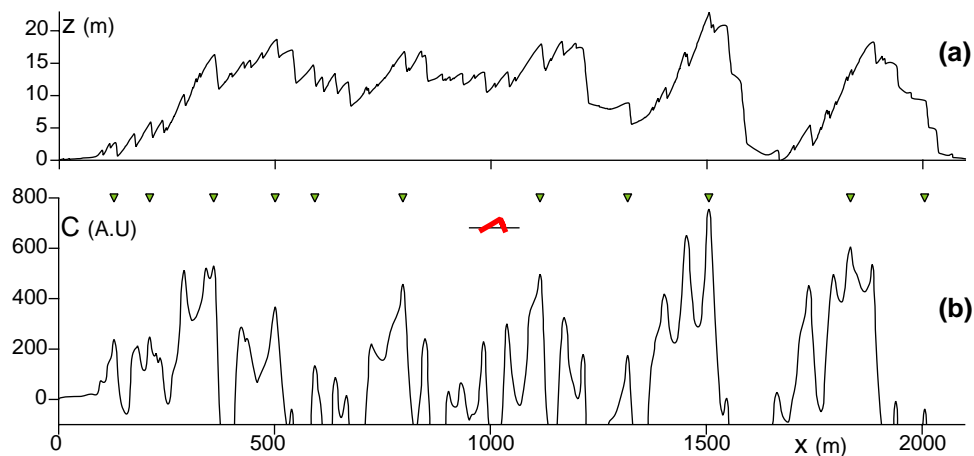

Figure 26: (a) Longitudinal profile of the transverse giant dune shown in figure 16 (blue dotted line). (b) Wavelet transform of this profile at the scale $L = 60$ m. The wavelet used is shown in red. The wavelet tranform $C(x)$ is the correlation of the profile and this wavelet. The value of C reflects the degree of similarity between the profile and the analysing wavelet. The maxima of the wavelet tranform (green triangles) are the points where C is maximum at the scale L, i.e. in a neighbourhood of size L on both sides. By construction, two such maxima are then at least separated by L. These maxima indicate the local presence of a structure of size larger (or equal) to L. The scale of a given structure is given by the end of the line connecting the maxima detected across a range of scales (see figure 4).

5   Symmetries of the wind regimes and the dune patterns

5.1   Symmetry principle

It is a general property of pattern emergence that shape and length-scales are not determined by the same effects. The selection of length-scales comes from physical mechanisms, while the pattern is governed by the symmetry of the forcing (boundary conditions or driving forces). Consider for instance a linear instability with a most unstable mode of wavelength λ. In a rectangular elongated cell, strips spaced at λ appear. In squared cells, a square pattern forms. In a circular cell, the pattern becomes hexagonal. Technically, this corresponds to the fact that the solution is a superposition of modes at the same wavelength but along different axis (figure 27). The boundary conditions determine the nature and number of such modes. In the case of dunes, the boundary conditions are replaced by the symmetries of the forcing (the wind regime).

5.2   Symmetry analysis

Figure 1 of the letter allows us to compare the symmetries of the wind regime and the dune pattern. In the case of a single wind direction, that direction is an axis of symmetry of the dune
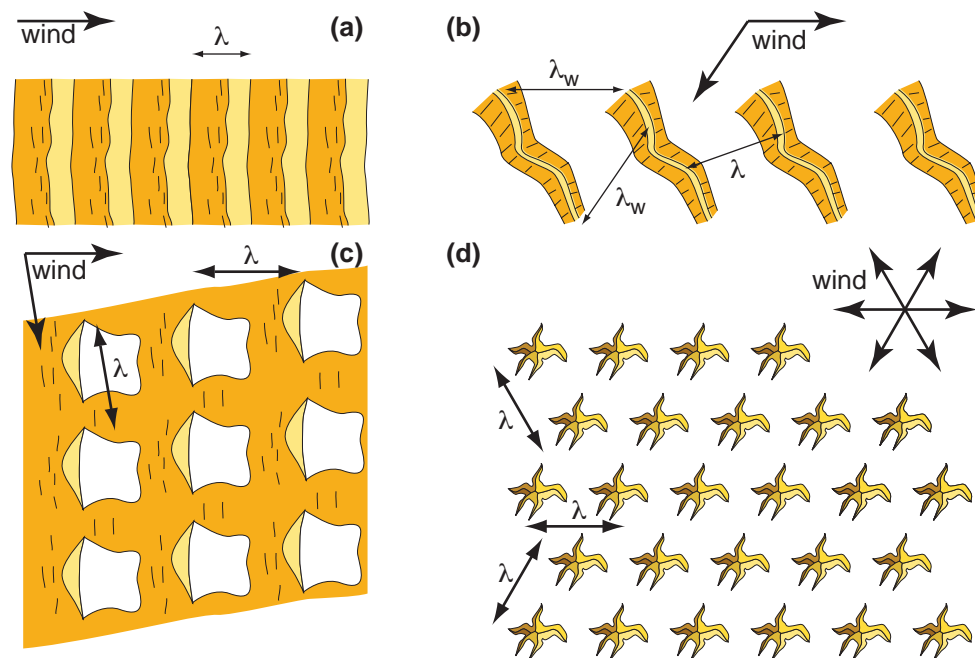

Figure 27: Selection of a pattern by mode superposition. (a) We assume that a single mode pattern appears under a unidirectional wind. (b) Under a bi-directional wind regime, a periodic array of uni-dimensional objects is still consistent with the symmetries. Such a pattern has a unique wavelength λ. A wind coming from one or the other direction sees a structure of period λ_w larger than λ. As an effect is at least as symmetric as its cause, the dunes must be along the bisector of the winds. This is the case of longitudinal dunes. (c) A bi-directional wind regime is also consistent with a bi-modal pattern (parallelogram lattice). This is the case of the dunes shown in figure 22. (d) Under a wind regime of three or six directions, the symmetries are consistent with a hexagonal pattern, that can be decomposed into three Fourier modes. This is the idealised case of star dunes.
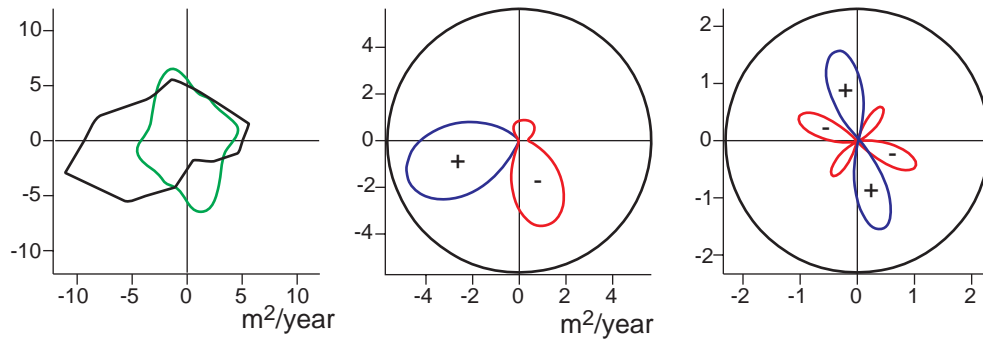
Figure 28: Comparison of the symmetries of the wind regime and the dune pattern in the Grand Erg Oriental (Algeria). (a) Polar diagrams of the transport rose (black) and the probability to find a neighbouring dune in a given direction (green). (b) Isotropic (black) and anisotropic (blue and red) components of the transport rose. (c) Same for neighbouring probablity.
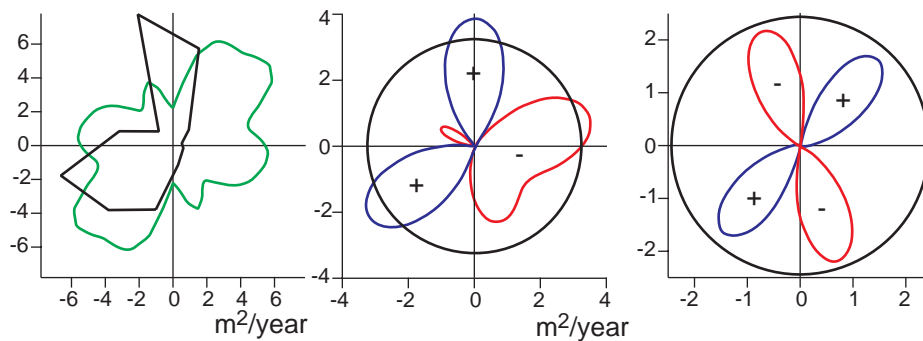

Figure 29: Comparison of the symmetries of the wind regime and the dune pattern in the Rub' al Khali desert (Saudi Arabia). Same colour codes as in figure 28.

pattern (transverse dunes or barchans). The case of longitudinal dunes is more complex as such a mono-mode pattern has a symmetry consistent with any wind direction. In the case shown in figure 1(c), the rose is composed by transverse and longitudinal winds, far from the ideal case discussed above in figure 27. The analysis is easier when isolated dunes can be defined, in the case of star dunes (as in Algeria, figure 28 and in Saudi Arabia, see figure 29)

For these three cases, we have analysed the sand transport roses and the probability to find one of the first three neighbouring dunes in a given direction α (angular structure function). These two quantities are plotted in polar coordinates in the panels (a). Note that the dune angular structure function is symmetric with respect to the origin, while the roses are not. In panels (b) and (c), these angular diagrams are decomposed into their isotropic (black circles) and anisotropic (blue for positive lobes and red for negative ones) components. This decomposition allows us to quantify the degree of anisotropy by comparing the size of the lobes to that of the corresponding circle. It also highlights the directions of anisotropy. For this purpose we have applied an angular low-pass filter on the anisotropic component.

The degree of anisotropy of the dune patterns (panels (c)) is well reflected by that of the wind regime (panels (b)). In figure 28, the weak anisotropy of the wind is visible along two orthogonal directions (positive and negative lobes). The dunes have a higher probability to have a neighbour in the direction transverse to the strong wind direction. This structure is reminiscent from the origin of these star dunes, probably formed by secondary instability of longitudinal dunes. This is consistent with the Fourier analysis of the dune pattern (see figure 11). In figure 29, the wind
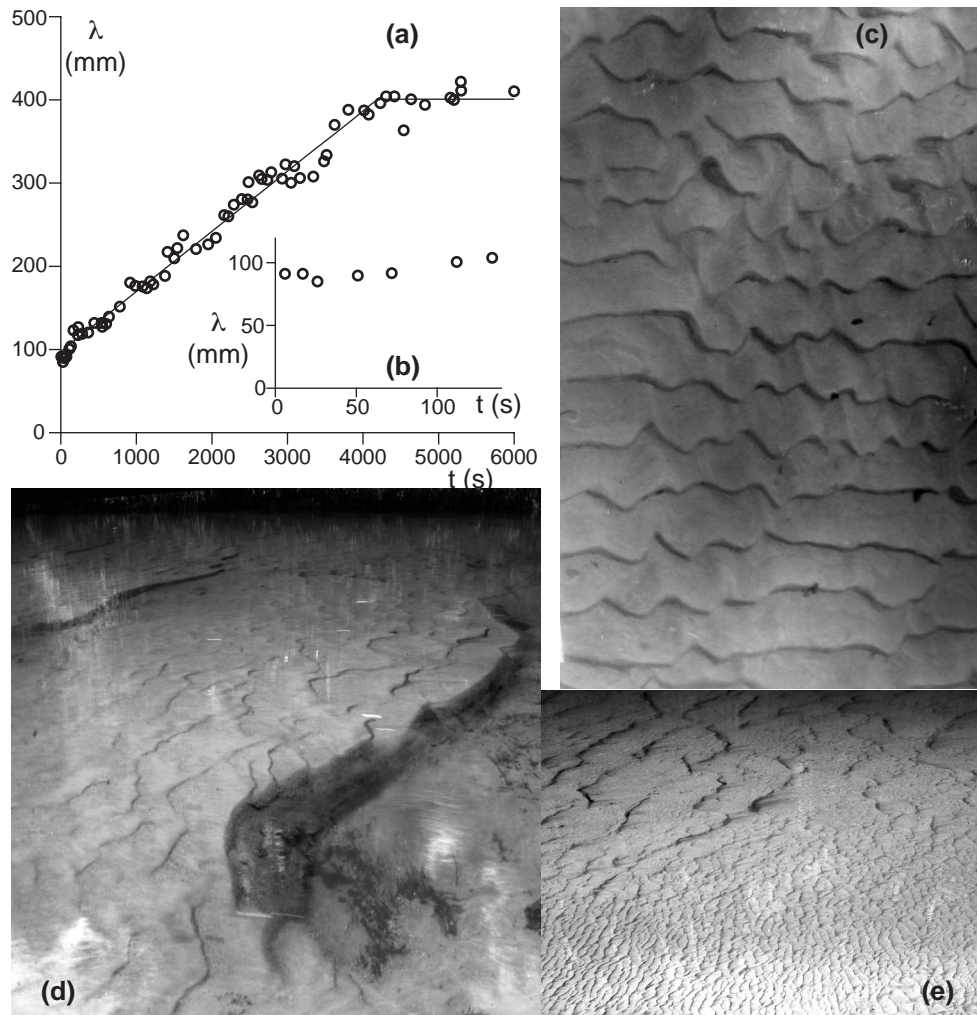
Figure 30: Dunes in the Leyre river (after [13, 14]). (a-c) Formation of dunes in a natural river, starting at $t = 0$ from a flat sand bed. The experiment was performed for a flow depth $H = 50$ cm, a Froude number $\phi = 0.28$ and a shear velocity $u_* = 4$ cm/s. The grain size is $d = 330 \pm 70$ μm. (a) Time evolution of the wavelength λ. The pattern coarsening starts after 150 s and stops after ~ 4000 s. (b) Same graph, but restricted to the linear regime (between $t = 0$ and $t = 150$ s). (c) The photograph shows the dunes of wavelength 40 cm formed after 6000 s. (d) Formation of giant dunes, starting from a flat sand bed. The experiment was performed for $H = 44$ cm, $\phi = 0.3$ and $u_* = 4$ cm/s. The sand is polydisperse: it is a mixture of sand grains of size $\sim 330 \pm 70$ μm, which cover 60% of the surface, and of coarse grains larger than 600 μm, which represent 40% of the surface – but 9% of the grains and 60% of the mass. The photograph shows 3 m long giant dunes with ~ 40 cm superimposed dunes. (e) Photograph of the river showing the sharp transition between dunes (zone of medium sand) and giant dunes (zone of medium and coarse sand mixed).
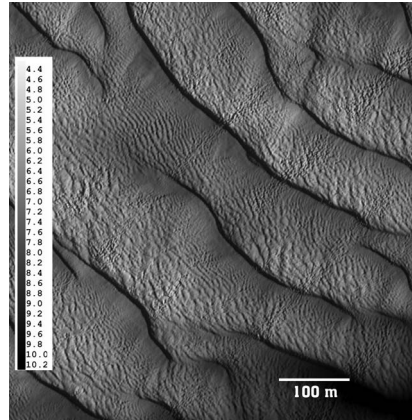
Figure 31: Echo sounder image of the bedforms in Rio Paraná, Argentina. The largest wavelength is around 100 m. The water depth is around 8 m. The flow is from top right to bottom left. This picture is from [16].

anisotropy reveals a nearly alternative wind regime (two positive lobes at $\simeq 120°$). The favoured direction of the dunes is normal to the bisector of the strong wind directions. This could correspond to a secondary instability of transverse giant dunes.

6   Other giant dunes

6.1   Giant dunes in rivers

Dunes develop in rivers whose bed, composed of grains (sand, gravels), is erodible. We refer the reader to our recent work on the formation of bedforms in rivers [13, 14]. Figure 30 shows that the amalgamation of superimposed bedforms – called ripples in this context – leads to a non-linear pattern coarsening. The bedform wavelength saturates at a value on the order of the water depth. These river dunes, whose size is determined by the flow depth, are thus the analogous of aeolian giant dunes.

While the sand composing aeolian sand dunes is usually well sorted by "aeolian sieving", the bed of a river can be at some places much more polydisperse. In the case of the Leyre river shown in figure 30, the polydispersity allows the pattern to coarsen much beyond the wavelength reached in the same flow conditions for a monodisperse bed. The very large river dunes, with wavelengths on the order of 10 times the depth – wavelengths much larger than that at which surface waves resonate with the relief – have no aeolian counterpart. A nice example of such giant river dunes is given by the echo sounder image of the Rio Paraná's bed (Argentina) performed by Parsons *et al.* [16], see figure 31. In this example, the wavelength of the bedforms varies from few meters to a hundred of meters, i.e. several times the water depth.

6.2   Snow giant dunes formed by katabatic winds in Antarctica

Aeolian dunes can form also with snow in Antarctica. They can form small barchans [11], but also giant dunes, as shown by NASA satellite images [17, 18, 19]. These giant dunes are only few meters high but several kilometers apart. The snow is transported by strong and almost permanent katabatic winds. An example of such dunes is displayed in figure 32(right).
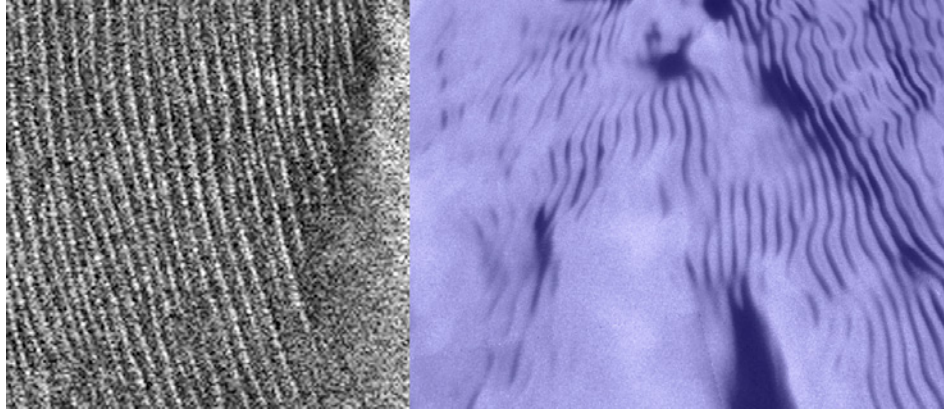
Figure 32: (left) Cassini RADAR Observations of dunes on Titan. The wavelength is around 1.7 km. This picture is from [20]. (right) Snow giant dunes in Antarctica. The wavelength is about 3 km. This picture is from [19].

6.3 Extraterrestrial dunes

Dunes of wavelength 1.7 km (figure 32(left)) have been discovered at the surface of Titan, during the Cassini-Huygens mission [20]. Given the few atmospheric and soil data available, and following the scaling law given in [11], we expect elementary dunes on Titan to be of the order of meters. The data provided by [21] give a well-mixed layer on the order of a kilometre or less. Therefore, whether these dunes are longitudinal or reversed, they can be classified as 'giant', in analogy with those on Earth.

7 Atmospheric boundary layer over a wavy bottom

In this section, we develop a weakly non-linear calculation for the description of the atmospheric turbulent flow over a wavy bottom. It extends former models that either ignore the turbulent fluctuations but include the free atmosphere [22] or treat the unbounded case using asymptotic matching [23, 24, 25], which assumes that the logarithm of the ratio of the dune length to the grain size is very large. Following the vertical structure of the ABL, we treat separately the well-mixed layer and the free atmosphere, in the spirit of the models used to describe mountain waves [27, 28, 29, 30]. The latter can be described analytically, and serves as upper boundary conditions for the integration of the differential equations describing the former.

7.1 Reynolds averaged description and Prandtl-like closure

We use the classical Boussinesq approximation for fluids whose densities have weak variations, e.g. due to temperature gradients. In this approach, ρ is taken constant (ρ_0) in all terms except for the gravity term [8]. Following the standard separation between average quantities and fluctuating ones (denoted with a prime), the equations governing the mean velocity field u_i can be written as:

$$\partial_i u_i = 0, \tag{34}$$

$$\partial_t u_i + u_j \partial_j u_i = -\partial_j \tau_{ij} - \partial_i p - \frac{\rho}{\rho_0} g_i, \tag{35}$$

where $\tau_{ij} = \overline{u_i' u_j'}$ is the Reynolds stress tensor. For the sake of simplicity, we omit the density factor in the pressure p and the stress tensor. Furthermore, as we treat the well-mixed layer here, we take a constant density $\rho = \rho_0$. We use here a Prandtl-like first order turbulence closure in which the distance to the bed determines the mixing length L, and the mixing frequency is

given by the strain rate modulus $|\dot{\gamma}| = \sqrt{\frac{1}{2}\dot{\gamma}_{ij}\dot{\gamma}_{ij}}$, where we have introduced the strain rate tensor $\dot{\gamma}_{ij} = \partial_i u_j + \partial_j u_i$.

Consider a homogeneous situation along the x-axis. The strain rate reduces to $\partial_z u_x$. With a shear stress that decreases linearly with height and vanishes at the capping height H, we can write:

$$\tau_{xz} = -\kappa^2 L^2 |\partial_z u_x| \partial_z u_x - \nu \partial_z u_x = -|u_*| u_* \left(1 - \frac{z}{H}\right), \tag{36}$$

where ν is the air viscosity. A simple and realistic choice is to introduce a mixing length L that tends to the aerodynamic roughness z_0 on the ground such as:

$$L^2 = (z + z_0)^2 \tag{37}$$

In the general case, we can write the stress tensor components as

$$\tau_{xz} = -\left(\kappa^2 L^2 |\dot{\gamma}| + \nu\right) \dot{\gamma}_{xz}, \tag{38}$$

$$\tau_{zz} = -\left(\kappa^2 L^2 |\dot{\gamma}| + \nu\right) \dot{\gamma}_{zz} + \frac{1}{3}\kappa^2 \chi^2 L^2 |\dot{\gamma}|^2, \tag{39}$$

and for simplicity again, we assume the isotropy of the tensor: $\tau_{xx} = \tau_{zz}$. In these expressions, κ and χ are two phenomenological constants. $\kappa \simeq 0.4$ is known as the von Kármán constant. The typical value of χ is between 2 and 3.

7.2 Expansion in amplitude of corrugation

We focus on 2D steady situations, i.e. geometries invariant along the y-direction. The Navier-Stokes equations (34) and (35) read

$$\partial_x u_x + \partial_z u_z = 0, \tag{40}$$

$$u_x \partial_x u_x + u_z \partial_z u_x = -\partial_x p - \partial_z \tau_{xz} - \partial_x \tau_{xx}, \tag{41}$$

$$u_x \partial_x u_z + u_z \partial_z u_z = -\partial_z p - \partial_z \tau_{zz} - \partial_x \tau_{zx} - g, \tag{42}$$

In expressions (38) and (39), the strain tensor components are

$$\dot{\gamma}_{xz} = \dot{\gamma}_{zx} = \partial_z u_x + \partial_x u_z, \tag{43}$$

$$\dot{\gamma}_{xx} = 2\partial_x u_x, \tag{44}$$

$$\dot{\gamma}_{zz} = 2\partial_z u_z = -\dot{\gamma}_{xx}, \tag{45}$$

$$|\dot{\gamma}|^2 = 2(\partial_x u_x)^2 + 2(\partial_z u_z)^2 + (\partial_z u_x + \partial_x u_z)^2. \tag{46}$$

For sufficiently small amplitudes, we can consider a bottom profile of the form $Z(x) = \zeta e^{ikx}$ without loss of generality. $\lambda = 2\pi/k$ is the wavelength of the bottom and $a = 2\zeta$ the amplitude of the corrugation. We shall use this standard notation with complex numbers for all quantities all throughout this section. However, note that, while computing non-linear contributions, one must temporarily go back to real notations (e.g. $Z = \zeta/2 \cos(kx)$). We introduce the dimensionless variable $\eta = kz$, the dimensionless roughness $\eta_0 = kz_0$, their sum $\ell = \eta + \eta_0$ and the Reynolds number:

$$\mathcal{R} = \frac{2\kappa^2 u_*}{k\nu}. \tag{47}$$

We also introduce the function $\mu(\eta)$ giving the profile at equilibrium:

$$\ell^2 |\mu'|\mu' + 2\mathcal{R}^{-1}\mu' + \frac{1}{\kappa^2}\left(\frac{\eta}{\eta_H} - 1\right) = 0, \tag{48}$$

or equivalently

$$\mu' = \frac{1}{\ell^2}\left[-\mathcal{R}^{-1} + \sqrt{\mathcal{R}^{-2} + \frac{\ell^2}{\kappa^2}\left(1 - \frac{\eta}{\eta_H}\right)}\right]. \tag{49}$$

We perform an expansion with respect to the dimensionless amplitude $k\zeta$ up to the (partial) third order:

$$u_x = u_* \left[\mu + (k\zeta)e^{ikx}U_1 + (k\zeta)^2 U_0 + (k\zeta)^2 e^{2ikx}U_2 + (k\zeta)^3 e^{ikx}U_3 \right], \tag{50}$$

$$u_z = u_* \left[(k\zeta)e^{ikx}W_1 + (k\zeta)^2 e^{2ikx}W_2 + (k\zeta)^3 e^{ikx}W_3 \right], \tag{51}$$

$$\tau_{xz} = -u_*^2 \left[1 - \frac{\eta}{\eta_H} + (k\zeta)e^{ikx}S_{t1} + (k\zeta)^2 S_{t0} + (k\zeta)^2 e^{2ikx}S_{t2} + (k\zeta)^3 e^{ikx}S_{t3} \right], \tag{52}$$

$$p + \tau_{zz} = p_H + gH\left(1 - \frac{\eta}{\eta_H} \right)$$
$$+ u_*^2 \left[(k\zeta)e^{ikx}S_{n1} + (k\zeta)^2 S_{n0} + (k\zeta)^2 e^{2ikx}S_{n2} + (k\zeta)^3 e^{ikx}S_{n3} \right], \tag{53}$$

where the U_i, W_i, S_{ti} and S_{ni} are functions of η. By 'partial', we mean that terms in e^{3ikx} are neglected. These harmonic third order terms give the first corrections to the linear solution. P_H is the pressure at the capping layer. Note: it can be shown that $W_0(\eta) = 0$. Therefore we do not include it into the following development.

Close the bottom, it is important that the mixing length retain its linear dependence on the distance to the ground. The bottom profile undulations should then be taken into account in the expression of L. However, introducing a term to get a vanishing L at the modulated capping layer is secondary. For the sake of simplicity, we then consider the following form for the mixing length:

$$(kL)^2 = \ell^2 - 2\ell(k\zeta)e^{ikx} + \frac{1}{2}(k\zeta)^2 + \frac{1}{2}(k\zeta)^2 e^{2ikx}. \tag{54}$$

The strain tensor components are:

$$\dot{\gamma}_{xx} = 2 \left[(k\zeta)e^{ikx}iU_1 + (k\zeta)^2 e^{2ikx}2iU_2 + (k\zeta)^3 e^{ikx}iU_3 \right], \tag{55}$$

$$\dot{\gamma}_{zz} = -\dot{\gamma}_{xx}, \tag{56}$$

$$\dot{\gamma}_{xz} = \mu' + (k\zeta)e^{ikx}(U_1' + iW_1) + (k\zeta)^2 U_0' + (k\zeta)^2 e^{2ikx}(U_2' + 2iW_2)$$
$$+ (k\zeta)^3 e^{ikx}(U_3' + iW_3), \tag{57}$$

so that the square of the strain modulus reads:

$$|\dot{\gamma}|^2 = \mu'^2 + (k\zeta)e^{ikx}\left[2\mu'(U_1' + iW_1) \right] + (k\zeta)^2 \left[2\mu'U_0' + \frac{1}{2}(U_1' + iW_1)(U_1'^* - iW_1^*) + 2U_1U_1^* \right]$$

$$+ (k\zeta)^2 e^{2ikx}\left[2\mu'(U_2' + 2iW_2) + \frac{1}{2}(U_1' + iW_1)^2 - 2U_1^2 \right] \tag{58}$$

$$+ (k\zeta)^3 e^{ikx}\left[2\mu'(U_3' + iW_3) + 2U_0'(U_1' + iW_1) + (U_1'^* - iW_1^*)(U_2' + 2iW_2) + 8U_1^*U_2 \right].$$

Taking the square root, we get:

$$|\dot{\gamma}| = \mu' + (k\zeta)e^{ikx}(U_1' + iW_1) + (k\zeta)^2 \left[U_0' + \frac{1}{\mu'}U_1U_1^* \right] + (k\zeta)^2 e^{2ikx}\left[U_2' + 2iW_2 - \frac{1}{\mu'}U_1^2 \right]$$

$$+ (k\zeta)^3 e^{ikx}\left[U_3' + iW_3 - \frac{1}{\mu'^2}U_1U_1^*(U_1' + iW_1) + \frac{1}{2\mu'^2}U_1^2(U_1'^* - iW_1^*) + \frac{4}{\mu'}U_1^*U_2 \right], \tag{59}$$

so that

$$(kL)^2|\dot{\gamma}| = \ell^2\mu' + (k\zeta)e^{ikx}\left[\ell^2(U_1' + iW_1) - 2\ell\mu' \right]$$

$$+ (k\zeta)^2 \left[\frac{1}{2}\mu' - \frac{\ell}{2}(U_1' + U_1'^* + iW_1 - iW_1^*) + \ell^2\left(U_0' + \frac{1}{\mu'}U_1U_1^* \right) \right]$$

$$+ (k\zeta)^2 e^{2ikx}\left[\frac{1}{2}\mu' - \ell(U_1' + iW_1) + \ell^2\left(U_2' + 2iW_2 - \frac{1}{\mu'}U_1^2 \right) \right]$$

$$
\begin{aligned}
+ \quad &(k\zeta)^3 e^{ikx} \left[\frac{1}{4} \left(2U_1' + U_1'^* + 2iW_1 - iW_1^* \right) \right. \\
- \quad &\ell \left(2U_0' + \frac{1}{\mu'} U_1 (2U_1^* - U_1) + U_2' + 2iW_2 \right) \\
+ \quad &\left. \ell^2 \left(U_3' + iW_3 - \frac{1}{\mu'^2} U_1 U_1^* (U_1' + iW_1) + \frac{1}{2\mu'^2} U_1^2 (U_1'^* - iW_1^*) + \frac{4}{\mu'} U_1^* U_2 \right) \right]. \quad (60)
\end{aligned}
$$

Finally, we can express the shear stress functions as follows:

$$
\begin{aligned}
S_{t1} &= \kappa^2 \left[2\mathcal{R}^{-1}(U_1' + iW_1) + 2\ell^2 \mu'(U_1' + iW_1) - 2\ell\mu'^2 \right], \quad (61) \\
S_{t0} &= \kappa^2 \left[2\mathcal{R}^{-1}U_0' + \frac{1}{2}\mu'^2 + \frac{\ell^2}{2}(U_1' + iW_1)(U_1'^* - iW_1^*) - \ell\mu'(U_1' + U_1'^* + iW_1 - iW_1^*) \right. \\
&\quad + \left. 2\ell^2 \mu' U_0' + \ell^2 U_1 U_1^* \right], \quad (62) \\
S_{t2} &= \kappa^2 \left[2\mathcal{R}^{-1}(U_2' + 2iW_2) + \frac{1}{2}\mu'^2 + \frac{\ell^2}{2}(U_1' + iW_1)^2 - 2\ell\mu'(U_1' + iW_1) \right. \\
&\quad + \left. 2\ell^2 \mu'(U_2' + 2iW_2) - \ell^2 U_1^2 \right], \quad (63) \\
S_{t3} &= \kappa^2 \left[2\mathcal{R}^{-1}(U_3' + iW_3) + -4\ell\mu' U_0' - \ell U_1 (2U_1^* - U_1) - 2\ell\mu'(U_2' + 2iW_2) + 2\ell^2 \mu'(U_3' + iW_3) \right. \\
&\quad + 4\ell^2 U_1^* U_2 + (U_1' + iW_1)\left(\mu' - \frac{\ell}{2}(U_1' + 2U_1'^* + iW_1 - 2iW_1^*) + 2\ell^2 U_0' \right) \\
&\quad + \left. \frac{1}{2}(U_1'^* - iW_1^*)\left(\mu' + 2\ell^2(U_2' + 2iW_2) \right) \right]. \quad (64)
\end{aligned}
$$

Solving the expressions of the shear stress functions for the U_i', we get:

$$
\begin{aligned}
U_1' &= \frac{1}{2(\mathcal{R}^{-1} + \ell^2 \mu')} \left[\frac{S_{t1}}{\kappa^2} - \left(-2\ell\mu'^2 \right) \right] - iW_1, \quad (65) \\
U_0' &= \frac{1}{2(\mathcal{R}^{-1} + \ell^2 \mu')} \left[\frac{S_{t0}}{\kappa^2} - \left(\frac{1}{2}\mu'^2 + \frac{\ell^2}{2}(U_1' + iW_1)(U_1'^* - iW_1^*) \right. \right. \\
&\quad - \left. \left. \ell\mu'(U_1' + U_1'^* + iW_1 - iW_1^*) + \ell^2 U_1 U_1^* \right) \right], \quad (66) \\
U_2' &= \frac{1}{2(\mathcal{R}^{-1} + \ell^2 \mu')} \left[\frac{S_{t2}}{\kappa^2} - \left(\frac{1}{2}\mu'^2 + \frac{\ell^2}{2}(U_1' + iW_1)^2 \right. \right. \\
&\quad - \left. \left. 2\ell\mu'(U_1' + iW_1) - \ell^2 U_1^2 \right) \right] - 2iW_2, \quad (67) \\
U_3' &= \frac{1}{2(\mathcal{R}^{-1} + \ell^2 \mu')} \left[\frac{S_{t3}}{\kappa^2} - \left[-4\ell\mu' U_0' - \ell U_1 (2U_1^* - U_1) - 2\ell\mu'(U_2' + 2iW_2) \right. \right. \\
&\quad + 4\ell^2 U_1^* U_2 + (U_1' + iW_1)\left(\mu' - \frac{\ell}{2}(U_1' + 2U_1'^* + iW_1 - 2iW_1^*) + 2\ell^2 U_0' \right) \\
&\quad + \left. \left. \frac{1}{2}(U_1'^* - iW_1^*)\left(\mu' + 2\ell^2(U_2' + 2iW_2) \right) \right] \right] - iW_3. \quad (68)
\end{aligned}
$$

The linear expansion of the Navier-Stokes equations gives rise to:

$$
\begin{aligned}
W_1' &= -iU_1, \quad (69) \\
S_{t1}' &= i\mu U_1 + \mu' W_1 + iS_{n1}, \quad (70) \\
S_{n1}' &= -i\mu W_1 + iS_{t1}. \quad (71)
\end{aligned}
$$

The second order expansion of the Navier-Stokes equations gives rise to two equations; one for the terms independent of x:

$$
\begin{aligned}
S_{t0}' &= \frac{1}{4}(W_1 U_1'^* + W_1^* U_1'), \quad (72) \\
S_{n0}' &= \frac{1}{4}i(U_1 W_1^* - U_1^* W_1) - \frac{1}{4}(W_1^* W_1' + W_1 W_1'^*) = \frac{1}{2}i(U_1 W_1^* - U_1^* W_1), \quad (73)
\end{aligned}
$$

and one for the terms proportional to e^{2ikx}:

$$W_2' = -2iU_2, \tag{74}$$

$$S_{t2}' = \mu'W_2 + \frac{1}{2}W_1U_1' + 2i\mu U_2 + \frac{1}{2}iU_1^2 + 2iS_{n2}, \tag{75}$$

$$S_{n2}' = -2i\mu W_2 - \frac{i}{2}U_1W_1 - \frac{1}{2}W_1W_1' + 2iS_{t2} = -2i\mu W_2 + 2iS_{t2}. \tag{76}$$

Note that S_{n0} does not enter the equation for S_{t0}' as its x-derivative is zero. Consequently, S_{n0} decouples from the rest of the problem. Finally, the third order expansion gives the correction to the e^{ikx} terms:

$$W_3' = -iU_3, \tag{77}$$

$$S_{t3}' = i\mu U_3 + iU_0U_1 + \frac{1}{2}iU_2U_1^* + \mu'W_3 + U_0'W_1 + \frac{1}{2}W_1^*U_2' + \frac{1}{2}W_2U_1'^* + iS_{n3}, \tag{78}$$

$$S_{n3}' = -i\mu W_3 - iU_0W_1 - iW_2U_1^* + \frac{1}{2}iU_2W_1^* - \frac{1}{2}W_1^*W_2' - \frac{1}{2}W_2W_1'^* + iS_{t3},$$

$$= -i\mu W_3 - iU_0W_1 - \frac{3}{2}iW_2U_1^* + \frac{3}{2}iU_2W_1^* + iS_{t3}. \tag{79}$$

The integration of the above set of differential equations (65)-(79) requires boundary conditions at the bottom and at the capping interface. For the latter, one first need to give a description of the stable free atmosphere.

7.3   Free atmosphere

The free atmosphere is a stress-free zone: the reference (homogeneous) state velocity vertical profile is uniform $\mu(\eta) = \mu(H) = \frac{1}{\kappa}\ln(1 + \eta_H/\eta_0) \equiv \mu_H$, so that $u_{FA} = u_*\mu_H$. Under the Boussinesq approximation, the Navier Stokes equations then read

$$\partial_x u_x + \partial_z u_z = 0, \tag{80}$$

$$u_x\partial_x u_x + u_z\partial_z u_x = -\partial_x p, \tag{81}$$

$$u_x\partial_x u_z + u_z\partial_z u_z = -\partial_z p - \frac{\rho}{\rho_0}g. \tag{82}$$

These equations must be supplemented by an equation describing the heat transfer. We assume that all transformations are adiabatic, hence $D\Theta/Dt = 0$ (see section 1). The equation of state of the air relates the potential temperature and the density (and the pressure). However, since under the Boussinesq approximation the main variations of the density come from those of the temperature (and not the pressure), one can write $D\rho/Dt = 0$ as the heat equation. In the steady case, it gives:

$$u_x\partial_x\rho + u_z\partial_z\rho = 0. \tag{83}$$

As before we start from a weakly non-linear expansion of the velocity and the pressure profiles in the presence of a wavy bottom:

$$u_x = u_*\left[\mu_H + (k\zeta)e^{ikx}U_1 + (k\zeta)^2U_0 + (k\zeta)^2e^{2ikx}U_2 + (k\zeta)^3e^{ikx}U_3\right], \tag{84}$$

$$u_z = u_*\left[(k\zeta)e^{ikx}W_1 + (k\zeta)^2e^{2ikx}W_2 + (k\zeta)^3e^{ikx}W_3\right], \tag{85}$$

$$p = p_H + \left[1 - \frac{\Delta\rho}{\rho_0}\right]gH\left(1 - \frac{\eta}{\eta_H}\right) + \frac{1}{2}N^2H^2\left(1 - \frac{\eta}{\eta_H}\right)^2$$

$$+ u_*^2\left[(k\zeta)e^{ikx}S_{n1} + (k\zeta)^2S_{n0} + (k\zeta)^2e^{2ikx}S_{n2} + (k\zeta)^3e^{ikx}S_{n3}\right]. \tag{86}$$

We also develop the density with respect to the amplitude:

$$\rho = \rho_0\left[1 - \frac{\Delta\rho}{\rho_0} + \frac{N^2H}{g}\left(1 - \frac{\eta}{\eta_H}\right)\right.$$

$$+ \left.(k\zeta)e^{ikx}R_1 + (k\zeta)^2R_0 + (k\zeta)^2e^{2ikx}R_2 + (k\zeta)^3e^{ikx}R_3\right]. \tag{87}$$

We introduce the so-called stream function Ψ, defined by $\partial_x \Psi = -u_z$ and $\partial_z \Psi = u_x$. This function is such that $\vec{u} \cdot \vec{\nabla} \Psi = 0$, so that the iso-contours $\Psi = \text{Cst}$ precisely show the streamlines. It is easy to show that it is given by $\Psi = \int u_x dz$, up to an arbitrary constant – setting $\Psi = 0$ on the bottom, the constant value of Ψ along a stream-line corresponds to the flux below it. In the x-homogeneous case, as $u_x = u_* \mu_H$, we have $\Psi \equiv u_* H \psi_b = u_* \mu_H (z - H) = u_* \mu_H H (\eta/\eta_H - 1)$. Like the other functions, we can express Ψ as:

$$\Psi = u_* H \left[\psi_b + (k\zeta)e^{ikx}\psi_1 + (k\zeta)^2 \psi_0 + (k\zeta)^2 e^{2ikx}\psi_2 + (k\zeta)^3 e^{ikx}\psi_3 \right]. \tag{88}$$

Note that the ψ_i are dimensionless. The relation $\partial_x \Psi = -u_z$ leads to the three following relations:

$$
\begin{aligned}
-i\eta_H \psi_1 &= W_1, \\
-2i\eta_H \psi_2 &= W_2, \\
-i\eta_H \psi_3 &= W_3.
\end{aligned}
$$

Similarly, the relation $\partial_z \Psi = u_x$ leads to:

$$
\begin{aligned}
\eta_H \psi_b' &= \mu_H, \\
\eta_H \psi_0' &= U_0,
\end{aligned}
$$

which is consistent with the above expression of ψ_b.

As the density is a passive scalar in this problem, it must be linearly related to the stream-function. The proportionality factor can be determined by comparing the linear terms in η in the respective expressions of ρ and Ψ. We get $\rho/\rho_0 = -\Psi N^2/(gu_*\mu_H)$. The density is thus directly related to the vertical motion as follows:

$$R_1 = -i\frac{N^2 H}{\mu_H g \eta_H} W_1, \tag{89}$$

$$R_0' = -\frac{N^2 H}{\mu_H g \eta_H} U_0, \tag{90}$$

$$R_2 = -i\frac{N^2 H}{2\mu_H g \eta_H} W_2, \tag{91}$$

$$R_3 = -i\frac{N^2 H}{\mu_H g \eta_H} W_3, \tag{92}$$

which is consistent with equation (83).

The expansion of the Navier-Stokes equations at the linear order gives:

$$W_1' = -iU_1, \tag{93}$$

$$0 = i\mu_H U_1 + iS_{n1}, \tag{94}$$

$$S_{n1}' = -i\mu_H W_1 - \frac{gH}{\eta_H u_*^2} R_1, \tag{95}$$

which leads to:

$$W_1'' = \left(1 - \frac{N^2}{k^2 u_*^2 \mu_H^2} \right) W_1 \tag{96}$$

The solutions are thus of the form $e^{q_1 \eta}$, with

$$q_1 = -\sqrt{1 - \frac{1}{\eta_B^2}} \quad \text{if} \quad \eta_B \geq 1, \tag{97}$$

$$q_1 = i\sqrt{\frac{1}{\eta_B^2} - 1} \quad \text{if} \quad \eta_B \leq 1, \tag{98}$$

where we have introduced the Brunt-Väisälä length $\mathcal{L}_B = \frac{u_* \mu_H}{N}$ and defined the dimensionless numbers $\eta_B = k\mathcal{L}_B$ and $\mathcal{B} = \mathcal{L}_B/H$. $\mathcal{B}$ is typically on the order of unity. There are two other solutions for q_1. However, the real mode $q_1 = +\sqrt{\ldots}$ should be rejected as the velocity correction should vanish when $z \to \infty$. Similarly, the imaginary mode $q_1 = -i\sqrt{\ldots}$ is not physically relevant as it corresponds to ways propagating energy from infinity [8]. Recalling that all stresses S_{ti} vanish in the FA, the linear solution then reads:

$$\vec{X}_1 \equiv \begin{pmatrix} U_1 \\ W_1 \\ S_{t1} \\ S_{n1} \end{pmatrix} = \begin{pmatrix} iq_1 \\ 1 \\ 0 \\ -i\mu_H q_1 \end{pmatrix} \xi_1 \, e^{q_1(\eta - \eta_H)}. \tag{99}$$

ξ_1 is related to the values of the functions U_1, W_1, S_{t1} and S_{n1} in $\eta = \eta_H$.

The second order expansion of the Navier-Stokes equations gives rise to five equations. Selecting the terms independent of x, we get a trivially verified equation ($W_1 U_1'^* + W_1^* U_1' = 0$) and a non-trivial one:

$$S_{n0}' = \frac{1}{2}i(U_1 W_1^* - U_1^* W_1) - \frac{gH}{\eta_H u_*^2} R_0 = -\frac{1}{2}(q_1 + q_1^*)W_1 W_1^* - \frac{gH}{\eta_H u_*^2} R_0. \tag{100}$$

The integration of the above differential equation requires to know the function $R_0(\eta)$, and thus $U_0(\eta)$ (see equation (90)). However, an additional assumption is required to get the latter, as it cannot be deduced from this systematic expansion. Recall that U_0 is the homogeneous correction to the mean velocity profile. In fact, any constant value for $U_0(\eta)$ is a solution of the problem. Two options are reasonable: either (i) $U_0(\eta) = 0$ which means that the FA is insensitive to the bottom corrugation so that the mean velocity profile is unchanged; or (ii) U_0 is continuous at the interface, which means that the whole FA feels the velocity correction in the same way as the top of the ML.

Selecting now the term in e^{2ikx}, we get:

$$W_2' = -2iU_2,$$
$$0 = \frac{1}{2}W_1 U_1' + 2i\mu_H U_2 + \frac{1}{2}iU_1^2 + 2iS_{n2} = 2i(\mu_H U_2 + S_{n2}),$$
$$S_{n2}' = -2i\mu_H W_2 - \frac{gH}{\eta_H u_*^2}R_2 = -2i\mu_H W_2 + i\frac{N^2}{2k^2 u_*^2 \mu_H}W_2. \tag{101}$$

Thus, the corresponding solutions are of the form $e^{q_2 \eta}$, with

$$q_2 = -\sqrt{4 - \frac{1}{\eta_B^2}} \quad \text{if} \quad 2\eta_B \geq 1, \tag{102}$$

$$q_2 = i\sqrt{\frac{1}{\eta_B^2} - 4} \quad \text{if} \quad 2\eta_B \leq 1. \tag{103}$$

The same remark as for q_1 concerning the modes $q_2 = +\sqrt{\ldots}$ and $q_2 = -i\sqrt{\ldots}$ applies here. The solution $\vec{X}_2 \equiv (U_2, W_2, S_{t2}, S_{n2})$ then reads:

$$\vec{X}_2 = \begin{pmatrix} \frac{i}{2}q_2 \\ 1 \\ 0 \\ -\frac{i}{2}\mu_H q_2 \end{pmatrix} \xi_2 \, e^{q_2(\eta - \eta_H)}. \tag{104}$$

Similar to ξ_1, x_2 is related to the values of the functions U_2, W_2, S_{t2} and S_{n2} in $\eta = \eta_H$.

Finally, the third order of the expansion gives the correction to the term in e^{ikx}:

$$W_3' = -iU_3, \tag{105}$$

$$0 = i\mu_H U_3 + iU_0 U_1 + \frac{1}{2}iU_2 U_1^* + U_0' W_1 + \frac{1}{2}W_1^* U_2' + \frac{1}{2}W_2 U_1'^* + iS_{n3}, \tag{106}$$

$$S_{n3}' = -\frac{gH}{\eta_H u_*^2}R_3 - i\mu_H W_3 - iU_0 W_1 - \frac{3}{4}(q_2 + 2q_1^*)W_2 W_1^*, \tag{107}$$

which can be rearranged into:

$$W_3' + iU_3 \quad = \quad 0, \tag{108}$$

$$\mu_H U_3 + S_{n3} \quad = \quad -iq_1 U_0 W_1 + \frac{1}{4}(2q_1^* + q_2)(q_1^* - q_2)W_1^* W_2, \tag{109}$$

$$S_{n3}' + i\mu_H W_3 - i\frac{N^2}{k^2 u_*^2 \mu_H}W_3 \quad = \quad -iU_0 W_1 - \frac{3}{4}(2q_1^* + q_2)W_1^* W_2. \tag{110}$$

The solution $\vec{X}_3 \equiv (U_3, W_3, S_{t3}, S_{n3})$ then reads:

$$\vec{X}_3 \quad = \quad \begin{pmatrix} iq_1\xi_3 + i\frac{1-q_1^2}{2\mu_H q_1}U_0\xi_1 + i\frac{1-q_1^2}{2\mu_H}U_0\xi_1(\eta - \eta_H) \\ \xi_3 + \frac{1-q_1^2}{2\mu_H q_1}U_0\xi_1(\eta - \eta_H) \\ 0 \\ -i\mu_H q_1\xi_3 - i\frac{q_1^2+1}{2q_1}U_0\xi_1 + i\frac{q_1^2-1}{2}U_0\xi_1(\eta - \eta_H) \end{pmatrix} e^{q_1(\eta - \eta_H)}$$

$$- \begin{pmatrix} -(q_1^* + q_2)(3 + q_1^{*2} - q_2^2) \\ i(3 + q_1^{*2} - q_2^2) \\ 0 \\ \mu_H[q_1^2(q_1^* - q_2) + 3(q_1^* + q_2)] \end{pmatrix} \frac{1}{4\mu_H q_2}\xi_1^*\xi_2\, e^{(q_1^* + q_2)(\eta - \eta_H)}, \tag{111}$$

where we have simplified the expression using the fact that q_1 is either real or purely imaginary. Again, ξ_3 is related to the values of all functions in η_H. These values will be involved in the expressions of the boundary conditions detailed below.

7.4   Boundary conditions on the bottom

Both components of the velocity should vanish at the bottom, i.e. for $\eta = kZ$. Recalling that we project all functions on the representation

$$f(x, \eta) = f_b(\eta) + (k\zeta)e^{ikx}f_1(\eta) + (k\zeta)^2 f_0(\eta) + (k\zeta)^2 e^{2ikx}f_2(\eta) + (k\zeta)^3 e^{ikx}f_3(\eta), \tag{112}$$

where f_b is the 'base' function, we can expand all $f_i(kZ)$ as

$$f_i(kZ) = f_i(0) + (kZ)f_i'(0) + (kZ)^2\frac{1}{2}f_i''(0) + (kZ)^3\frac{1}{6}f_i'''(0). \tag{113}$$

With $Z = \zeta e^{ikx}$, the second and third powers of kZ read:

$$(kZ)^2 \quad = \quad (k\zeta)^2\frac{1}{2}(1 + e^{2ikx}), \tag{114}$$

$$(kZ)^3 \quad = \quad (k\zeta)^3\frac{3}{4}e^{ikx}. \tag{115}$$

We then get

$$\begin{aligned} f(x, kZ) \quad = \quad & f_b(0) + (k\zeta)e^{ikx}\left[f_1(0) + f_b'(0)\right] \\ + \quad & (k\zeta)^2\left[f_0(0) + \frac{1}{4}f_b''(0) + \frac{1}{4}f_1(0) + \frac{1}{4}f_1^{*\prime}(0)\right] \\ + \quad & (k\zeta)^2 e^{2ikx}\left[f_2(0) + \frac{1}{4}f_b''(0) + \frac{1}{2}f_1'(0)\right] \\ + \quad & (k\zeta)^3 e^{ikx}\left[f_3(0) + \frac{1}{8}f_b'''(0) + f_0'(0) + \frac{1}{2}f_2'(0) + \frac{1}{4}f_1''(0) + \frac{1}{8}f_1^{*\prime\prime}(0)\right]. \end{aligned} \tag{116}$$

The above formulae apply for the computation of $u_x(x, kZ)$, with $f_b(\eta) = \mu(\eta) = \frac{1}{\kappa}\ln(1 + \eta/\eta_0)$. The condition $u_x(x, kZ) = 0$ then leads to:

$$U_1(0) \quad = \quad -\frac{1}{\kappa\eta_0}, \tag{117}$$

$$U_0(0) = \frac{1}{4\kappa\eta_0^2} - \frac{1}{4}U_1'(0) - \frac{1}{4}U_1'^*(0), \tag{118}$$

$$U_2(0) = \frac{1}{4\kappa\eta_0^2} - \frac{1}{2}U_1'(0), \tag{119}$$

$$U_3(0) = -\frac{1}{4\kappa\eta_0^3} - U_0'(0) - \frac{1}{2}U_2'(0) - \frac{1}{4}U_1''(0) - \frac{1}{8}U_1''^*(0). \tag{120}$$

Similarly, for $u_z(x, kZ) = 0$ (for which $f_b = 0$), we get:

$$W_1(0) = 0, \tag{121}$$

$$W_2(0) = -\frac{1}{2}W_1'(0) = \frac{i}{2}U_1(0) = -\frac{i}{2\kappa\eta_0}, \tag{122}$$

$$W_3(0) = -\frac{1}{4}W_1''(0) - \frac{1}{8}W_1''^*(0) - \frac{1}{2}W_2'(0) = \frac{i}{4}U_1'(0) - \frac{i}{8}U_1'^*(0) + iU_2(0). \tag{123}$$

7.5 Boundary conditions at the capping layer

The capping layer is described as an infinitesimaly thin interface between the well-mixed layer below and the free atmosphere above. We call its altitude $H + \Delta(x)$. When needed, we shall specify below η_H^+ and η_H^-, or $H + \Delta^+$ and $H + \Delta^-$, in order to distinguish between the interface viewed from the FA or from the ML respectively.

When the bottom is flat, $\Delta = 0$. When some corrugation is present, we write

$$k\Delta = (k\zeta)e^{ikx}\delta_1 + (k\zeta)^2\delta_0 + (k\zeta)^2 e^{2ikx}\delta_2 + (k\zeta)^3 e^{ikx}\delta_3, \tag{124}$$

where the δ_i are (complex) numbers. It is easy to see that $\delta_0 = 0$. This identity is indeed related to the fact that this interface is a streamline whose value (the flux below it) must be the same with and without corrugation. This property does not allow for an additional term whose contribution does not vanish on average (over x). In the same spirit as the previous subsection, we can expand the non linear terms:

$$(k\Delta)^2 = (k\zeta)^2\frac{1}{2}\delta_1\delta_1^* + (k\zeta)^2 e^{2ikx}\frac{1}{2}\delta_1^2 + (k\zeta)^3 e^{ikx}\delta_2\delta_1^*, \tag{125}$$

$$(k\Delta)^3 = (k\zeta)^3 e^{ikx}\frac{3}{4}\delta_1^2\delta_1^*. \tag{126}$$

This then leads to:

$$\begin{aligned}
f(x, \eta_H + k\Delta) &= f_b(\eta_H) + (k\zeta)e^{ikx}\left[f_1(\eta_H) + f_b'(\eta_H)\delta_1\right] \\
&+ (k\zeta)^2\left[f_0(\eta_H) + \frac{1}{4}f_b''(\eta_H)\delta_1\delta_1^* + \frac{1}{4}f_1'(\eta_H)\delta_1^* + \frac{1}{4}f_1^{*\prime}(\eta_H)\delta_1\right] \\
&+ (k\zeta)^2 e^{2ikx}\left[f_2(\eta_H) + f_b'(\eta_H)\delta_2 + \frac{1}{4}f_b''(\eta_H)\delta_1^2 + \frac{1}{2}f_1'(\eta_H)\delta_1\right] \\
&+ (k\zeta)^3 e^{ikx}\left[f_3(\eta_H) + f_b'(\eta_H)\delta_3 + \frac{1}{2}f_b''(\eta_H)\delta_1^*\delta_2 + \frac{1}{8}f_b'''(\eta_H)\delta_1^2\delta_1^* + f_0'(\eta_H)\delta_1\right. \\
&+ \left.\frac{1}{2}f_2'(\eta_H)\delta_1^* + \frac{1}{2}f_1^{*\prime}(\eta_H)\delta_2 + \frac{1}{4}f_1''(\eta_H)\delta_1\delta_1^* + \frac{1}{8}f_1^{*\prime\prime}(\eta_H)\delta_1^2\right].
\end{aligned} \tag{127}$$

The first condition we wish to impose at the capping layer is that the density drops by a constant amount $\Delta\rho$, i.e. $\rho(x, \eta_H + k\Delta^+) = \rho_0 - \Delta\rho$. Using the above expression (127) for $f = \rho$ as well as the relation $R_1(\eta_H^+) = \frac{N^2}{gk}\delta_1$ we get:

$$R_0(\eta_H^+) = -\frac{1}{4}R_1'(\eta_H^+)\delta_1^* - \frac{1}{4}R_1^{*\prime}(\eta_H^+)\delta_1 = -\frac{N^2}{4gk}(q_1 + q_1^*)\delta_1\delta_1^*. \tag{128}$$

Note that, although they can be computed the same way, the expressions giving the functions R_2 and R_3 are not useful for our purpose.

The second point, already mentionned, is that the interface is a streamline, so that the stream function should be constant along the it. This statement should be true both from the point of view of the FA, and from that of the ML. Within the FA, the stream-line condition is $\Psi(x, \eta_H + k\Delta^+) = u_* H \psi_b$. Using expression (127) for $f = \Psi$ we then get:

$$\xi_1 = W_1(\eta_H^+) = i\mu_H \delta_1, \tag{129}$$

$$\xi_2 = W_2(\eta_H^+) = 2i\mu_H \delta_2 - q_1 \delta_1 \xi_1, \tag{130}$$

$$\xi_3 = W_3(\eta_H^+) + \frac{i(3 + q_1^{*2} - q_2^2)}{4\mu_H q_2} \xi_1^* \xi_2$$

$$= i\mu_H \delta_3 + \frac{1}{2}\delta_2 q_1^* \xi_1^* + i\delta_1 U_0(\eta_H) - \frac{1}{4}\delta_1^* q_2 \xi_2 - \frac{1}{4}\delta_1 \delta_1^* q_1^2 \xi_1 + \frac{1}{8}\delta_1^2 q_1^{*2} \xi_1^*$$

$$+ \frac{i(3 + q_1^{*2} - q_2^2)}{4\mu_H q_2} \xi_1^* \xi_2. \tag{131}$$

These three equations define the amplitude of modulation in the free atmosphere layer for a given Δ. Note that the very same equation set could have been derived from the relation $u_z = u_x \partial_x \Delta$, which is an equivalent definition of streamlines. Similarly, the streamline nature of the capping layer expressed within the well-mixed layer reads:

$$W_1(\eta_H^-) = i\mu_H \delta_1, \tag{132}$$

$$W_2(\eta_H^-) = 2i\mu_H \delta_2 - \delta_1 W_1'(\eta_H^-) + \frac{i}{2}\mu_H' \delta_1^2 = 2i\mu_H \delta_2 + i\delta_1 U_1(\eta_H^-) + \frac{i}{2\kappa(\eta_H + \eta_0)} \delta_1^2, \tag{133}$$

$$W_3(\eta_H^-) = i\mu_H \delta_3 - \frac{1}{2}\delta_2 W_1^{*'}(\eta_H^-) + i\delta_1 U_0(\eta_H^-) - \frac{1}{2}\delta_1^* W_2'(\eta_H^-) - \frac{1}{4}\delta_1 \delta_1^* W_1''(\eta_H^-)$$

$$- \frac{1}{8}\delta_1^2 W_1^{*''}(\eta_H^-) + \frac{i}{2}\mu_H' \delta_1^* \delta_2 + \frac{i}{8}\mu_H'' \delta_1^2 \delta_1^*$$

$$= i\mu_H \delta_3 + \frac{i}{2}\delta_2 U_1^*(\eta_H^-) + i\delta_1 U_0(\eta_H^-) + \frac{i}{2}\delta_1^* U_2(\eta_H^-) + \frac{i}{4}\delta_1 \delta_1^* U_1'(\eta_H^-)$$

$$+ \frac{i}{8}\delta_1^2 U_1^{*'}(\eta_H^-) + \frac{i}{2\kappa(\eta_H + \eta_0)} \delta_1^* \delta_2 - \frac{i}{8\kappa(\eta_H + \eta_0)^2} \delta_1^2 \delta_1^*. \tag{134}$$

This equation set can be thought of as defining the position of the interface, i.e. δ_1, δ_2 and δ_3, once the velocity field in the ML is known.

Finally, in agreement with our choice for the mixing length, we require that turbulence vanishes at the interface. This condition is consistent with the fact that the FA is a stress-free zone. As a consequence, the stress tensor is diagonal in $\eta_H + k\Delta$. Therefore, we wish to impose:

$$\tau_{xz}(x, \eta_H + k\Delta^-) = 0, \tag{135}$$

$$p(x, \eta_H + k\Delta^-) = p(x, \eta_H + k\Delta^+). \tag{136}$$

With the use of the above expression (127) with the S_{ti}, we get for the first of these two conditions:

$$S_{t1}(\eta_H^-) = \frac{1}{\eta_H}\delta_1, \tag{137}$$

$$S_{t0}(\eta_H^-) = -\frac{1}{4}S_{t1}'(\eta_H)\delta_1^* - \frac{1}{4}S_{t1}^{*'}(\eta_H)\delta_1, \tag{138}$$

$$S_{t2}(\eta_H^-) = \frac{1}{\eta_H}\delta_2 - \frac{1}{2}S_{t1}'(\eta_H)\delta_1, \tag{139}$$

$$S_{t3}(\eta_H^-) = \frac{1}{\eta_H}\delta_3 - \frac{1}{2}S_{t1}^{*'}(\eta_H)\delta_2 - S_{t0}'(\eta_H)\delta_1 - \frac{1}{2}S_{t2}'(\eta_H)\delta_1^* - \frac{1}{4}S_{t1}''(\eta_H)\delta_1\delta_1^*$$

$$- \frac{1}{8}S_{t1}^{*''}(\eta_H)\delta_1^2. \tag{140}$$

Again, with the use of expression (127) with $f = p$, we get the pressure at $z = H + \Delta$ in the ML:

$$
\begin{aligned}
\frac{p(x, \eta_H + k\Delta^-) - p_H}{u_*^2} &= (k\zeta)e^{ikx}\left[S_{n1}(\eta_H^-) - \frac{g}{ku_*^2}\delta_1\right] \\
&+ (k\zeta)^2\left[S_{n0}(\eta_H^-) + \frac{1}{4}S_{n1}'(\eta_H^-)\delta_1^* + \frac{1}{4}S_{n1}^*{}'(\eta_H^-)\delta_1\right] \\
&+ (k\zeta)^2 e^{2ikx}\left[S_{n2}(\eta_H^-) - \frac{g}{ku_*^2}\delta_2 + \frac{1}{2}S_{n1}'(\eta_H^-)\delta_1\right] \\
&+ (k\zeta)^3 e^{ikx}\left[S_{n3}(\eta_H^-) - \frac{g}{ku_*^2}\delta_3 + S_{n0}'(\eta_H^-)\delta_1 + \frac{1}{2}S_{n2}'(\eta_H^-)\delta_1^*\right. \\
&+ \left.\frac{1}{2}S_{n1}^*{}'(\eta_H^-)\delta_2 + \frac{1}{4}S_{n1}''(\eta_H^-)\delta_1\delta_1^* + \frac{1}{8}S_{n1}^*{}''(\eta_H^-)\delta_1^2\right]. \qquad (141)
\end{aligned}
$$

In the FA, the pressure at $z = H + \Delta$ reads:

$$
\begin{aligned}
\frac{p(x, \eta_H + k\Delta^+) - p_H}{u_*^2} &= (k\zeta)e^{ikx}\left[-i\mu_H q_1\xi_1 - \left(1 - \frac{\Delta\rho}{\rho_0}\right)\frac{g}{ku_*^2}\delta_1\right] \qquad (142) \\
&+ (k\zeta)^2\left[S_{n0}(\eta_H^+) + \left(\frac{N}{2ku_*}\right)^2\delta_1\delta_1^* + \frac{1}{4}S_{n1}'(\eta_H^+)\delta_1^* + \frac{1}{4}S_{n1}^*{}'(\eta_H^+)\delta_1\right] \\
&+ (k\zeta)^2 e^{2ikx}\left[-\frac{i}{2}\mu_H q_2\xi_2 - \left(1 - \frac{\Delta\rho}{\rho_0}\right)\frac{g}{ku_*^2}\delta_2 + \left(\frac{N}{2ku_*}\right)^2\delta_1^2\right. \\
&+ \left.\frac{1}{2}S_{n1}'(\eta_H^+)\delta_1\right] \\
&+ (k\zeta)^3 e^{ikx}\left[-i\mu_H q_1\xi_3 - i\frac{q_1^2 + 1}{2q_1}\xi_1 U_0(\eta_H^+)\right. \\
&+ \frac{(2q_1^* + q_2)[q_1^2(q_1^* - q_2) + 3(q_1^* + q_2)]}{4[q_1^2 - (q_1^* + q_2)^2)]}\xi_1^*\xi_2 \\
&- \left(1 - \frac{\Delta\rho}{\rho_0}\right)\frac{g}{ku_*^2}\delta_3 + \left(\frac{N}{2ku_*}\right)^2\delta_1^*\delta_2 + S_{n0}'(\eta_H^+)\delta_1 \\
&+ \left.\frac{1}{2}S_{n2}'(\eta_H^+)\delta_1^* + \frac{1}{2}S_{n1}^*{}'(\eta_H^+)\delta_2 + \frac{1}{4}S_{n1}''(\eta_H^+)\delta_1\delta_1^* + \frac{1}{8}S_{n1}^*{}''(\eta_H^+)\delta_1^2\right].
\end{aligned}
$$

Balancing the upper and lower pressures, and replacing the ξ_i as well as the several functions $f(\eta_H^+)$ by their expressions, we finally get for the last boundary conditions:

$$
S_{n1}(\eta_H^-) = \mu_H^2\left(q_1 + \frac{1}{\eta_H\phi^2}\right)\delta_1, \qquad (143)
$$

$$
S_{n0}(\eta_H^-) = \frac{1}{4}\mu_H^2\left((q_1 - q_1^*)^2 + \frac{1}{\eta_B^2}\right)\delta_1\delta_1^* - \frac{1}{4}S_{n1}'(\eta_H^-)\delta_1^* - \frac{1}{4}S_{n1}^*{}'(\eta_H^-)\delta_1 \qquad (144)
$$

$$
S_{n2}(\eta_H^-) = \mu_H^2\left(q_2 + \frac{1}{\eta_H\phi^2}\right)\delta_2 + \frac{1}{2}\mu_H^2\left(q_1(q_1 - q_2) + \frac{1}{2\eta_B^2}\right)\delta_1^2 - \frac{1}{2}S_{n1}'(\eta_H^-)\delta_1 \qquad (145)
$$

$$
\begin{aligned}
S_{n3}(\eta_H^-) &= \mu_H^2\left(q_1 + \frac{1}{\eta_H\phi^2}\right)\delta_3 + \mu_H U_0(\eta_H^+)\frac{3q_1^2 + 1}{2q_1}\delta_1 \qquad (146) \\
&+ \frac{1}{2}\mu_H^2\left(q_2^2 + q_1^2 - q_1(q_1^* + q_2) + \mathcal{Q} + \frac{1}{\eta_B^2}\right)\delta_1^*\delta_2 \\
&- \frac{1}{2}\mu_H^2\left(q_1 + q_1^* + \frac{1}{2}q_1 q_2(q_2 - q_1) + \frac{1}{4}q_1^2(q_1 - q_1^*) + \frac{1}{2}q_1\mathcal{Q} - \frac{1}{2\eta_B^2}(q_1 + q_1^*)\right)\delta_1^2\delta_1^* \\
&- \left(S_{n0}'(\eta_H^-)\delta_1 + \frac{1}{2}S_{n2}'(\eta_H^-)\delta_1^* + \frac{1}{2}S_{n1}^*{}'(\eta_H^-)\delta_2 + \frac{1}{4}S_{n1}''(\eta_H^-)\delta_1\delta_1^* + \frac{1}{8}S_{n1}^*{}''(\eta_H^-)\delta_1^2\right),
\end{aligned}
$$

where we have introduced the Froude number

$$\phi = \frac{u_* \mu_H}{\sqrt{\frac{\Delta \rho}{\rho_0} gH}} \,, \tag{147}$$

and with

$$\mathcal{Q} = \frac{q_1(3 + q_1^2 - q_2^2) - (q_1^2(q_1^* - q_2) + 3(q_1^* + q_2))}{q_2} \,. \tag{148}$$

In the main text, we also use the notation $\mathcal{S} \equiv \phi^2$ to refer to a Shields number. Its typical value is around unity. As q_1 is either purely real or imaginary, we can express $\mathcal{Q}$ as

$$\mathcal{Q} = -3 - q_1 q_2 + q_1^2 \quad \text{if} \quad \eta_B \geq 1, \tag{149}$$

$$\mathcal{Q} = -3 - q_1 q_2 + q_1^2 + 2q_1 \frac{3 + q_1^2}{q_2} \quad \text{if} \quad \eta_B \leq 1. \tag{150}$$

With the velocities U_i and W_i given at the bottom (equations (117)-(123)), the stresses S_{ti} and S_{ni} given at the capping layer (equations (137)-(140) and (143)-(146)), as well as the definition of the interface (equations (132)-(134)), one can solve the differential equation set derived in the previous subsection.

An essential output of this integration is the shear stress as well as the pressure on the bottom. We define the coefficients A_i and B_i as:

$$\tilde{S}_{ti}(0) = A_i + iB_i, \tag{151}$$

where, in accordance with the relation (116), the $\tilde{S}_{ti}(0)$ and $\tilde{S}_{ni}(0)$ are given by the different expressions between brakets at each order of the expansion for $f = \tau_{xz}$ and $f = p + \tau_{zz}$ respectively.

These quantities can be related to the growth rate σ of an erodible wavy bed of wavelength λ. For that purpose, the main ingredient regarding sediment transport is the saturation length ℓ_{sat} [10, 11]; it reads:

$$\sigma(k) = Qk^2 \frac{B_1 - A_1 k \ell_{\text{sat}}}{1 + (k \ell_{\text{sat}})^2} \,, \tag{152}$$

where Q is the saturated flux over a flat bed – its value depends on the wind strength. ℓ_{sat} is on the order of few meters. The maximum value of sigma occurs for $k_s \ell_{\text{sat}} \simeq B_1/A_1$.

In the non-linear regime, one can compute the amplitude at which the shear stress and thus the sand flux are in phase with the giant dune relief. We cannot use the standard expansion a la Ginzburg-Landau close to the instability threshold as there is no such threshold. We thus make the approximation that well-developed dunes can still be approximated by sinusoidal shapes i.e. that hydrodynamics is insensitive to the details of shape. Technically, we neglect the triad-mode interaction and look only at the effect of a particular Fourier mode on itself, through the generation of zero mode and first harmonic. We then predict the aspect ratio of the dune as

$$\frac{a}{\lambda} = \frac{2\zeta}{\lambda} = \frac{1}{\pi}\sqrt{-B_1/B_3} \,. \tag{153}$$

References

[1] R.W. Hyland and A. Wexler,
Formulations for the Thermodynamic Properties of the saturated Phases of H_2O from 173.15K to 473.15K,
ASHRAE Trans. **89**(2A), pp 500-519 (1983).

[2] IGRA web site: `http://www.ncdc.noaa.gov/oa/cab/igra/`.

[3] I. Durre, R.S. Vose and D.B. Wuertz,
Overview of the Integrated Global Radiosonde Archive,
J. Climate **19**, 53 (2006).

[4] Weather archives: `http://meteo.infospace.ru/wcarch/html/index.sht`.

[5] R.B. Stull,
An introduction to boundary layer meteorology,
Kluwer Academic Publishers (1988).

[6] J.R. Garrat,
The atmospheric boundary layer,
Cambridge University Press (1994).

[7] Y. Shao,
Physics and modelling of wind erosion,
Kluwer Academic Publishers (2000).

[8] D.J. Tritton,
Physical fluid dynamics,
Van Nostrand Reinhold Compagny, Wokingham (1977).

[9] B. Andreotti, P. Claudin and S. Douady,
Selection of dune shapes and velocities: a two dimensional modelling,
Eur. Phys. J. B **28**, 341 (2002).

[10] H. Elbelrhiti, P. Claudin and B. Andreotti,
Field evidence for surface-wave-induced instability of sand dunes,
Nature **437**, 720 (2005).

[11] P. Claudin and B. Andreotti,
A scaling law for aeolian dunes on Mars, Venus, Earth, and for subaqueous ripples,
Earth and Planetary Science Letters **252**, 30 (2006).

[12] H. Elbelrhiti, B. Andreotti and P. Claudin,
Barchan dune corridors: field characterization and investigation of control parameters,
J. Geophys. Res. **113**, F02S15 (2008).

[13] Fourrière A., Claudin P. and Andreotti B., *Bedforms in a turbulent stream. Part 1: Turbulent flow over topography*, submitted to J. Fluid Mech., arXiv:0708.2823 (2009).

[14] Fourrière A., Claudin P. and Andreotti B., *Bedforms in a turbulent stream. Part 2: Formation of ripples by primary linear instability and of dunes by non-linear pattern coarsening*, submitted to J. Fluid Mech., arXiv:0805.3417 (2009).

[15] Andersen K.H., Chabanol M.-L., van Hecke M., *Dynamical models for sand ripples beneath surface waves*, Phys. Rev. E **63**, 066308 (2001).

[16] D.R. Parsons, J.L. Best, O. Orfeo, R.J. Hardy, R. Kostaschuk, and S.N. Lane,
Morphology and flow fields of three-dimensional dunes, Rio Paraná, Argentina: Results from simultaneous multibeam echo sounding and acoustic Doppler current profiling,
J. Geophys. Res. **110**, F04S03 (2005).

[17] M.A. Fahnestock, T.A. Scambos, C.A. Shuman, R.J. Arthern, D.P. Winebrenner and R. Kwok,
Snow megadune fields on the east antarctic plateau: extreme atmosphere-ice interaction,
Geophys. Res. Lett. **27**, 3719 (2000).

[18] M. Frezzotti, S. Gandolfi and S. Urbini,
Snow megadunes in Antarctica: Sedimentary structure and genesis,
J. Geophys. Res. **107**, NO. D18, 4344 (2002).

[19] M. Fahnestock, T. Scambos, T. Haran, and R. Bauer,
AWS data: characteristics of snow megadunes and their potential effect on ice core interpretation,
Boulder, Colorado USA: National Snow and Ice Data Center. Digital media (2006),
see also `http://nsidc.org/antarctica/megadunes/`.

[20] R.D. Lorenz *et al.*,
The Sand Seas of Titan: Cassini RADAR Observations of Longitudinal Dunes,
Science **312**, 724 (2006).

[21] T. Tokano, F. Ferri, G. Colombatti, T. Mäkinen, and M. Fulchignoni,
Titan's planetary boundary layer structure at the Huygens landing site,
J. Geophys. Res. **111**, E08007 (2006).

[22] D. J. Carruthers and T.W. Choularton,
Air-Flow over Hills of Moderate Slope,
Quart. J. R. Met. Soc. **108**, 603 (1982).

[23] P.S. Jackson, and J.C.R. Hunt,
Turbulent Wind Flow over a Low Hill,
Quart. J. R. Met. Soc. **101**, 929 (1975).

[24] J.C.R. Hunt, S. Leibovich and K.J. Richards,
Turbulent wind flows over low hills,
Quart. J. R. Met. Soc. **114**, 1435 (1988).

[25] J.C.R. Hunt, K.J. Richards and P.W.M. Brighton,
Stably stratified shear flow over low hills,
Quart. J. R. Met. Soc. **114**, 859 (1988).

[26] K.J. Richards, and P.A. Taylor,
A non-linear model of finite depth flow over sand waves,
Geophys. J. R. Astr. Soc. **65** 103 (1981).

[27] R.D. Sharman and M.G. Wurtele,
Ship and lee waves,
J. Atm. Sc. **40**, 396 (1983).

[28] R.R. Long,
A theory of mixing in a stably stratified fluid,
J. Fluid. Mech. **84**, 113 (1978).

[29] D.R. Durran,
Two-layer solutions to Long's equation for vertically propagating mountain waves: how good is linear theory?,
Quart. J. R. Met. Soc. **118**, 415 (1992).

[30] W. Weng, L. Chan, P.A. Taylor and D. Xu,
Modelling stably stratified boundary-layer flow over low hills,
Quart. J. R. Met. Soc. **123**, 1841 (1997).